

1 **Revealing the Causes of Groundwater Level Dynamics in Seasonally Frozen Soil Zones**

2 **Using Interpretable Deep Learning Models**

3 Han Li <sup>a,b,c</sup>, Hang Lyu <sup>a,b,c\*</sup>, Boyuan Pang <sup>a,b,c</sup>, Xiaosi Su <sup>a,b,c</sup>, Weihong Dong <sup>a,b,c</sup>, Yuyu Wan <sup>a,b,c</sup>,

4 Tiejun Song <sup>a,b,c</sup>, Xiaofang Shen <sup>a,b,c</sup>

5 <sup>a</sup>Key Laboratory of Groundwater Resources and Environment, Ministry of Education, Jilin  
6 University, Changchun 130026, China

7 <sup>b</sup>Jilin Provincial Key Laboratory of Water Resources and Environment, Jilin University,  
8 Changchun 130026, China

9 <sup>c</sup>Institute of Water Resources and Environment, Jilin University, Changchun,130021, China

10 \*Corresponding author

11 Hang Lyu

12 E-mail: lvhangmail@163.com

13      **Abstract**

14      Accurately characterizing groundwater level dynamics in seasonal frozen soil regions is  
15      of great significance for water resource management and ecosystem protection. To this end,  
16      this study proposes a new interpretable deep learning method to reveal the underlying causes  
17      of groundwater level dynamics on the basis of groundwater level simulation. Using the  
18      Songnen Plain in China as the study area and daily data from 138 monitoring wells,  
19      groundwater levels are simulated with an Long Short-Term Memory (LSTM) model, and the  
20      Expected Gradients (EG) method is employed to quantitatively identify the dominant factors  
21      and mechanisms of different groundwater level variation types. The results show that the LSTM  
22      model performs well on the test set, with the Nash-Sutcliffe Efficiency (NSE) exceeding 0.7 at  
23      81.88% of the monitoring sites, effectively capturing the temporal dynamics of groundwater  
24      levels. At the annual scale, three typical groundwater level variation types are identified:  
25      precipitation infiltration–evaporation type (29.0%), precipitation infiltration–runoff type  
26      (18.1%), and extraction type (52.9%). Corresponding to the seasonal frozen-thaw period,  
27      groundwater level dynamics are classified into “V”-shaped (38.4%), continuous decline  
28      (23.2%), and continuous rise (38.4%) types. Quantitative analysis using the EG method  
29      indicates that air temperature, precipitation, and snow thickness are the primary controlling  
30      factors of the “V”-shaped dynamics, reflecting the regulatory role of the frozen-thaw process  
31      on groundwater levels. When the initial groundwater level depth at the beginning of the freezing  
32      period is shallower than the sum of the frozen-thaw influence depth and the capillary rise height,  
33      a hydraulic connection is established between soil water and groundwater, resulting in typical  
34      “V”-shaped fluctuations. Conversely, when the depth exceeds this critical threshold, the frozen-  
35      thaw process cannot significantly influence the aquifer, and groundwater dynamics are mainly  
36      manifested as continuous rise or continuous decline, driven respectively by groundwater  
37      extraction and water level recovery following precipitation recharge. This study establishes an

38 integrated framework of “simulation–classification–interpretation,” which not only improves  
39 the accuracy of groundwater level dynamic simulation and prediction but also provides new  
40 methods and perspectives for revealing the underlying mechanisms. The findings offer  
41 theoretical support and technical basis for regional groundwater resource management in cold  
42 regions.

43 **Keywords:** Freezing-thawing process; Groundwater level dynamics; Seasonally frozen plain;  
44 Interpretable deep learning models

45 **1. Introduction**

46 Groundwater level is a crucial indicator reflecting the water balance status of groundwater  
47 systems, and its dynamic changes reveal the evolving trends of regional hydrological processes.  
48 In terms of water resource management, monitoring groundwater level depth helps managers  
49 understand changes in groundwater storage, optimize water extraction schemes, and prevent  
50 resource depletion caused by overexploitation (Hao et al., 2014; Yang, 2012). Regarding  
51 ecosystem protection, fluctuations in groundwater level depth directly affect regional  
52 ecological patterns. Excessively low water levels may lead to wetland desiccation and  
53 biodiversity loss, while rapid rises can cause soil salinization and vegetation degradation (Singh  
54 et al., 2012). Relevant studies have also practically validated the significance of groundwater  
55 level prediction. For example, Liu et al. (2022) demonstrated in the lower Tarim River that  
56 machine learning-based groundwater level prediction models can quantitatively reveal current  
57 and future groundwater changes, clarifying the critical role of ‘ecological water conveyance’  
58 in regional ecological restoration. Therefore, in-depth identification of the controlling  
59 mechanisms behind groundwater level depth variations and achieving high-precision  
60 spatiotemporal simulation are of great significance for promoting sustainable groundwater  
61 resource utilization and ecological environment protection (Yi et al., 2022).

62 Seasonally frozen soil areas are widely distributed globally. In China, they cover more  
63 than half of the total land area, mainly in the northwest and northeast regions where water  
64 scarcity is a prominent issue (Wang et al., 2019). Unlike non-frozen soils, seasonally frozen  
65 soil is a unique water-soil system that contains ice, and changes in the ice content are  
66 accompanied by the dynamic storage of liquid water and dynamic changes in heat (Wu et al.,  
67 2023). The movement and storage behavior of groundwater in these regions differ from those  
68 in warm, non-frozen areas (Ireson et al., 2013), as the freeze-thaw process results in more  
69 frequent interactions between soil water and groundwater (Daniel and Staricka, 2000; Lyu et

70 al., 2022; Lyu et al., 2023; Miao et al., 2017). This leads to significant differences in the causes  
71 of groundwater level dynamics between the freeze–thaw and non-freeze–thaw periods in  
72 seasonally frozen soil areas, making it more challenging to accurately simulate the regional  
73 groundwater levels.

74 Current models used for simulating groundwater level dynamics can generally be  
75 categorized into two groups: physical models and machine learning models (Ao et al., 2021).  
76 Most physical models are based on hydrodynamic processes and water balance principles, and  
77 are capable of accurately representing the physical mechanisms of groundwater systems.  
78 Therefore, they possess irreplaceable advantages in characterizing groundwater flow and  
79 uncovering hydrological processes such as recharge, runoff, and discharge. However, in areas  
80 with complex geological structures or highly heterogeneous aquifer systems, the construction,  
81 parameter calibration, and validation of physical models typically require large amounts of  
82 high-resolution geological, hydrological, and hydraulic data. These requirements make  
83 physical modeling challenging to implement and time-consuming (Raghavendra N and Deka,  
84 2014). Hence, there are few simulation studies on regional-scale groundwater level dynamics  
85 in seasonally frozen soil areas. In comparison, machine learning models have demonstrated  
86 significant advantages in simulating groundwater levels. These models explore the nonlinear  
87 relationships between inputs (such as meteorological and topographic data) and outputs  
88 (groundwater level) without the need to consider internal physical mechanisms (Rajaee et al.,  
89 2019), nor do they require predefined parameters such as hydraulic characteristics or boundary  
90 conditions (Ao et al., 2021). Despite this, machine learning models typically outperform  
91 physical models in terms of simulation accuracy, particularly in medium-to-long-term  
92 simulation studies (Demissie et al., 2009; Ebrahimi and Rajaee, 2017; Fienen et al., 2016;  
93 Rahman et al., 2020). One of the most successful deep learning architectures for modeling  
94 dynamic hydrological variables is the long short-term memory (LSTM) network (Jing et al.,

95 2023; Wu et al., 2021). The LSTM model, which is an improved version of the recurrent neural  
96 network (RNN), can more effectively capture long-term dependencies in time-series data  
97 (Hochreiter and Schmidhuber, 1997). In the seasonally frozen soil regions of Northwest China,  
98 14 years of continuous groundwater level simulations have shown that the LSTM model can  
99 effectively handle long-term data and accurately simulate groundwater levels in seasonally  
100 frozen soil areas (Zhang et al., 2018).

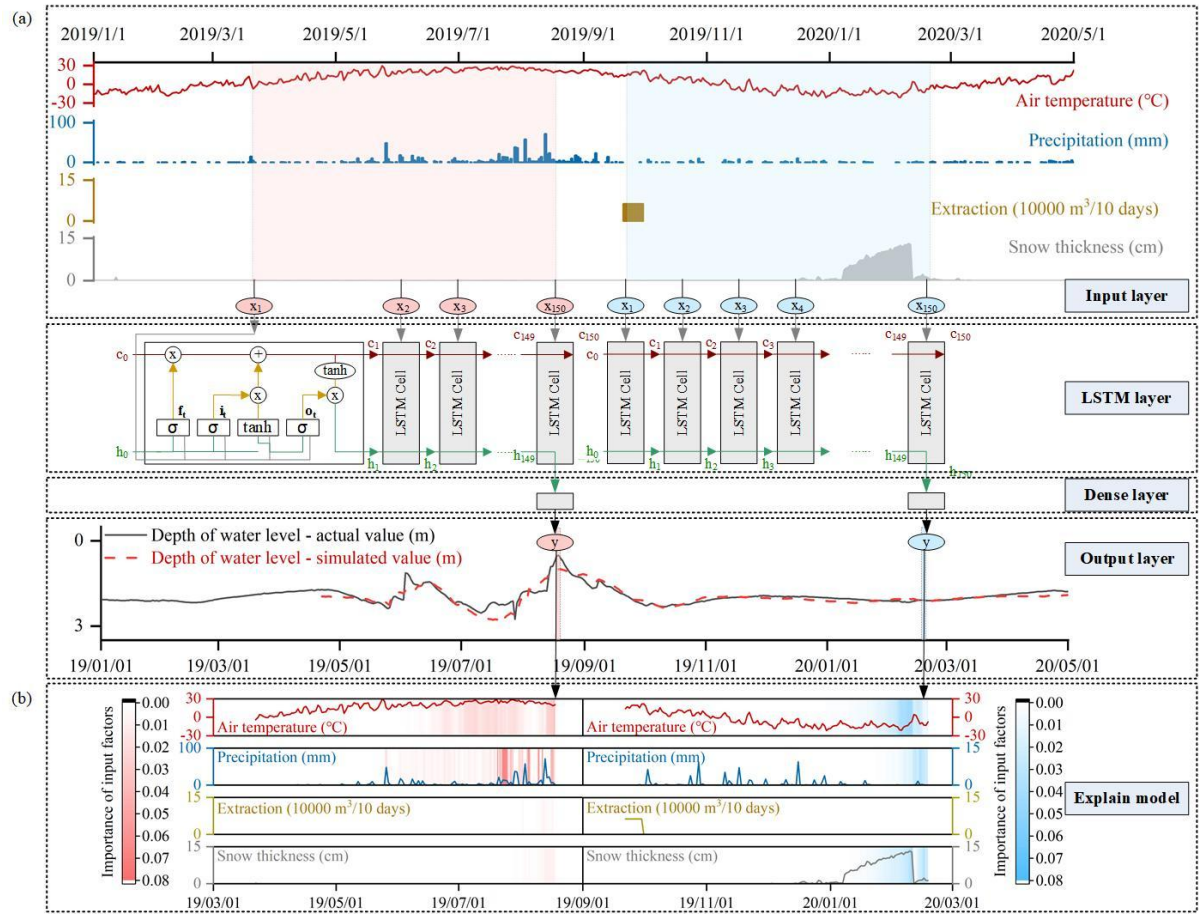
101 Although numerous studies have demonstrated the accuracy and predictive power of data-  
102 driven models in hydrological fields, these models are essentially black boxes and cannot  
103 explicitly explain the underlying physical processes and mechanisms (Zhou and Zhang, 2023).  
104 To address this limitation, researchers have proposed various methods to interpret deep learning  
105 models. Two widely used methods in groundwater research are the expected gradient (EG)  
106 method (Jiang et al., 2022) and the Shapley additive explanations (SHAP) algorithm (Lundberg  
107 and Lee, 2017). The broad application of the SHAP method is mainly attributed to its ability to  
108 reveal, from a local perspective, the contribution of each input variable to the corresponding  
109 model output at each time step (Wang et al., 2022) and, from a global perspective, the overall  
110 influence of input variables on the model output over the entire simulation period (Liu et al.,  
111 2022; Niu et al., 2023). However, the limitation of the SHAP method is that its interpretation  
112 of input factors is static and independent, making it ineffective in capturing the complex  
113 interactions between groundwater levels and long-term recharge and discharge dynamics. In  
114 contrast, the EG method (Jiang et al., 2022) calculates the EG values of the input variables over  
115 a specified time range, allowing for a better quantification of the impact of dynamic input  
116 variables on output variables at a particular time. This capability theoretically makes the EG  
117 method advantageous in groundwater level simulations with dynamic characteristics,  
118 particularly in explaining the temporal effects of meteorological changes on groundwater level  
119 across different periods. Nevertheless, there are currently no dedicated studies on the use of the

120 EG method to explain the causes of groundwater level dynamics, and its effectiveness in  
121 understanding the relatively complex mechanisms of groundwater level dynamics in seasonally  
122 frozen soil areas requires further validation.

123 In this study, the seasonally frozen soil area of the Songnen Plain in Northeastern China  
124 was taken as an example. Through an in-depth analysis of three years of continuous monitoring  
125 data from phreatic wells in this region, combined with meteorological, hydrological, and soil  
126 texture data, the LSTM model was used to simulate the groundwater level dynamics. The  
127 reverse interpretation technique, i.e., the EG method, was applied to explore the decision  
128 principles of the deep learning model in simulating water levels during the non-freeze–thaw  
129 and freeze–thaw periods, thus revealing the mechanisms behind groundwater level dynamics  
130 across different periods in seasonally frozen soil areas. The research findings can demonstrate  
131 and extend the application of interpretable deep learning models in the groundwater field,  
132 providing essential support for groundwater resource assessment and ecological environment  
133 protection in seasonally frozen soil areas.

134 **2. Data and methodology**

135 Figure 1 shows the workflow of this study, including three main steps. First, the LSTM  
136 model is used to establish a nonlinear relationship between meteorological factors, human  
137 activities, and groundwater level depths (Fig. 1a). The daily air temperature, precipitation,  
138 extraction volume, and snow depth were used as input variables to predict the groundwater  
139 level depths. Subsequently, the EG method (Jiang et al., 2022) was applied to the trained LSTM  
140 model to obtain the EG scores of the input factors at different time steps. The EG scores  
141 quantify the influence of the meteorological inputs (air temperature, precipitation, and snow  
142 depth) and human activities (extraction volume) on the groundwater level depths during the  
143 simulation process (Fig. 1b). Finally, the causes of groundwater level dynamics during the non-  
144 freeze–thaw and freeze–thaw periods in seasonally frozen soil areas were identified.



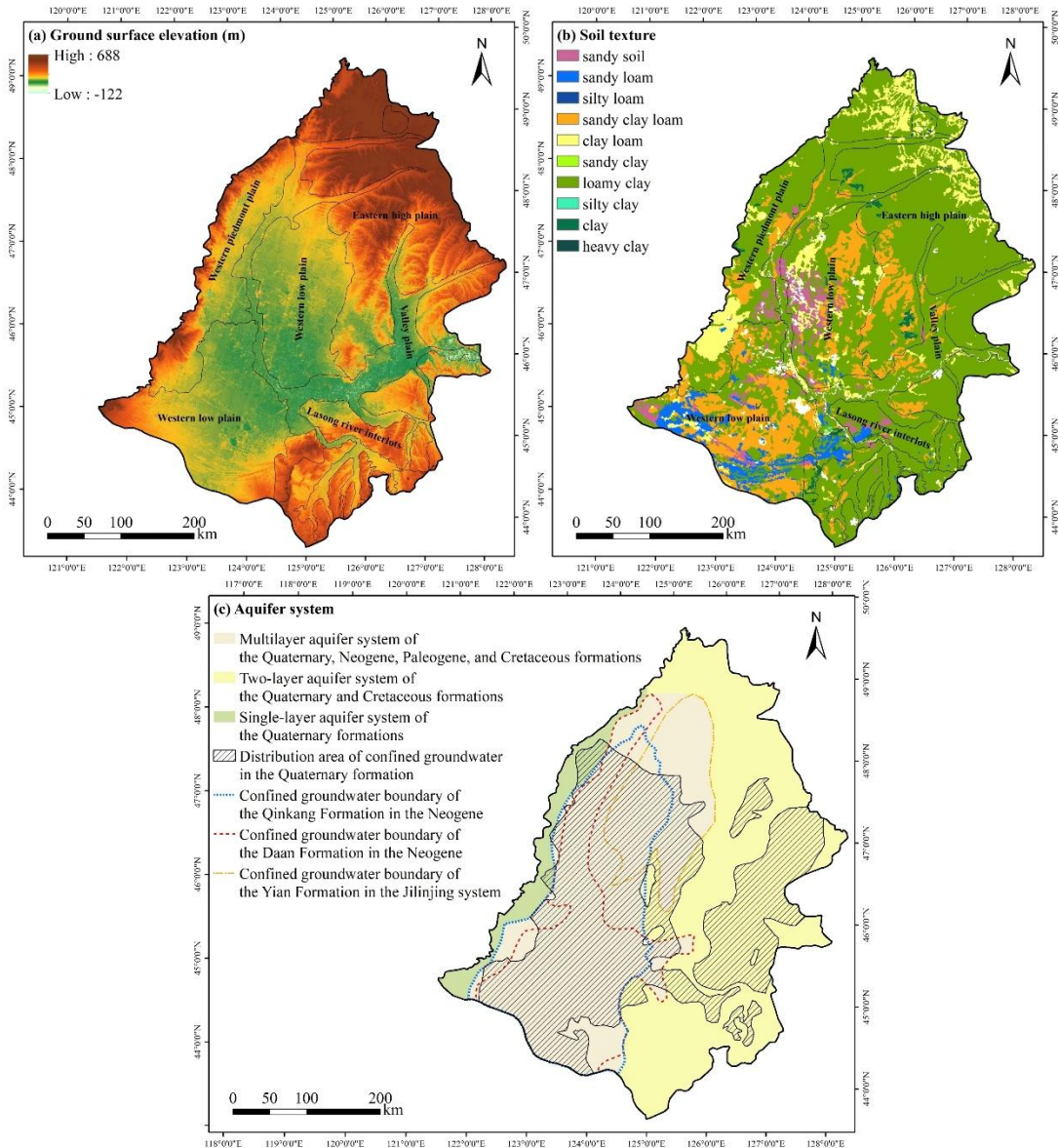
145

146 **Fig. 1.** Workflow of this study: (a) Model structure of the LSTM model, (b) EG scores of input  
147 factors during the non-freeze–thaw and freeze–thaw periods.

148 **2.1. Study area**

149 The Songnen Plain is one of the three major plains in Northeast China. It is higher on the  
150 periphery and lower at the center, with a total area of 182,800 km<sup>2</sup> (Fig. 2a). The study area is  
151 surrounded by hills and mountains in the west, north, and east of the Greater and Lesser Xingan,  
152 Zhangguangcai, and Changbai Mountains, respectively, and is connected to the West Liaohe  
153 Plain by the micro-uplifted Songliao watershed in the south. The Songnen Plain primarily  
154 comprises the eastern high plain, western piedmont sloping plain, western low plain, and valley  
155 plain (Fig. 2a). The soil texture in the region mainly includes sandy loam, sandy clay loam,  
156 clay loam, and loamy clay (Fig. 2b). The climate in the area can be mainly characterized by  
157 two main types: first, it features a typical East Asian continental monsoon climate with hot,

158 rainy summers and cold, dry winters; second, although the distribution of the climatic factors  
159 in the Songnen Plain is significantly influenced by latitude, there is a distinct east–west  
160 difference, with arid conditions in the west and humid conditions in the east (Li et al., 2022).  
161 The long-term average temperature of the Songnen Plain is 3.8 °C, the long-term average  
162 precipitation is 484.57 mm, and the long-term average evaporation is 1,498.1 mm. The frost-  
163 free period ranges from 115 to 160 days. Freezing starts in mid-October from north to south,  
164 and thawing begins in April from south to north. The freezing depth ranges from 1.5 to 2.4 m  
165 (Zhao et al., 2009). The area is crisscrossed by rivers, with the Songhua River, Nenjiang River,  
166 and their tributaries forming a centripetal drainage system. The lower reaches of the Nenjiang  
167 River and Taoer River, as well as the Second Songhua River, flow through the central plain  
168 from the north, west, and southeast, respectively. The aquifer system in the Songnen Plain,  
169 China, consists of multiple aquifers ranging from the Cretaceous, Paleogene, and Neogene to  
170 the Quaternary. Among them, the Quaternary aquifer, whose distribution range is slightly  
171 smaller than that of the Cretaceous aquifer, is the main groundwater exploitation layer in the  
172 region and the aquifer in which the groundwater studied in this paper is located (Fig. 2c).



173

174 **Fig. 2.** Spatial distribution of the ground surface elevation (a), topography (b) and aquifer  
 175 system (c) in the Songnen Plain, China.

176 **2.2. Dataset and selection of representative groundwater level values**

177 To simulate the dynamic changes in the groundwater level in seasonally frozen soil areas  
 178 and to analyze the driving mechanisms of groundwater level dynamics during freezing and  
 179 non-freezing periods, this study primarily used dynamic observational data from 2018 to 2021,  
 180 including precipitation, air temperature, snow depth, groundwater extraction volume, and  
 181 groundwater levels, as well as static data such as ground surface elevation and soil texture. The  
 182 precipitation and air temperature data were obtained from the “ERA5 hourly data on single

183 levels from 1979 to present" dataset, provided by the European Centre for Medium-Range  
184 Weather Forecasts (ECMWF). ERA5 is the fifth-generation re-analysis of the global climate  
185 and weather data with a spatial resolution of  $0.25^\circ \times 0.25^\circ$  and an hourly temporal resolution.  
186 Daily snow depth data were sourced from the National Tibetan Plateau Data Center  
187 (<http://data.tpdc.ac.cn>), with a spatial resolution of 25 km. The temporal and spatial resolution  
188 of the groundwater extraction volume data was enhanced based on the spatial distribution and  
189 water demand of major crops in the Songnen Plain, along with the precipitation data.  
190 Groundwater level data from 138 phreatic wells were provided by the China Geological  
191 Environment Monitoring Institute, while surface elevation data with a spatial resolution of 30  
192 m were obtained from the Geospatial Data Cloud (<https://www.gscloud.cn/search>). Soil texture  
193 data were sourced from the Resource and Environment Science and Data Center, compiled  
194 from a 1:1,000,000 soil type map and soil profile data collected during the second national soil  
195 survey of China.

196 In the Songnen Plain, approximately 70% of groundwater extraction is used for  
197 agricultural irrigation; therefore, in this study, groundwater extraction was approximated based  
198 on crop water deficits. Using spatial distribution data of the region's major crops, ten-day  
199 period crop water requirements, and precipitation data, we estimated groundwater extraction  
200 at a fine resolution, ultimately generating ten-day period groundwater extraction data with a  
201 spatial resolution of  $25 \text{ km} \times 25 \text{ km}$ . Specifically, based on the water requirements of the main  
202 crops (rice, soybean, and maize), we calculated the total crop water demand for each ten-day  
203 period within each grid cell. These values were then weighted according to the crop planting  
204 area to obtain the total water demand per grid. By comparing precipitation with crop water  
205 demand, we determined whether precipitation could meet the crop water needs. When  
206 precipitation was sufficient, crops relied entirely on natural rainfall, and the effective  
207 precipitation equaled the water demand. When precipitation was insufficient, effective

208 precipitation was limited by actual rainfall, and the remaining crop water deficit was assumed  
209 to be supplemented by other water sources. Finally, the difference between crop water demand  
210 and effective precipitation was calculated as the crop water deficit, which was assumed to be  
211 primarily supplied by groundwater. This allowed us to approximate ten-day period  
212 groundwater extraction. To ensure consistency with the temporal resolution of other variables  
213 used for model training, the ten-day period data were converted to daily averages by dividing  
214 by the number of days in each period.

215 To identify the causes of groundwater level dynamics during freezing and non-freezing  
216 periods, representative groundwater levels were selected for analysis using the EG method at  
217 different time periods. Based on the annual pattern of the groundwater level dynamics,  
218 groundwater levels during the non-freezing period are influenced by human activities, flood-  
219 season precipitation, and other factors, leading to greater fluctuations compared with that  
220 observed in the freezing period. Therefore, selecting extreme values (either maximum or  
221 minimum) as representative groundwater levels can effectively capture the peak or trough of  
222 the groundwater level, reflecting the most significant state of groundwater recharge or  
223 discharge during this period. Based on this, the trends in the groundwater level were analyzed  
224 to identify the different dynamic characteristics during the non-freezing period. If the  
225 groundwater level shows an overall uptrend, the maximum value represents the peak of the  
226 recharge process; if it shows a downtrend, the minimum value reflects the maximum extent of  
227 discharge.

228 However, during the freezing period, groundwater level fluctuations are relatively small,  
229 and extreme values do not respond significantly to external factors. During this period,  
230 groundwater levels may be influenced by soil freezing and thawing processes. Therefore, the  
231 groundwater levels at critical moments of soil freezing and thawing were chosen as  
232 representative values to more accurately reflect the response of groundwater level to

233 environmental changes. During the freezing period, after the “Beginning of Winter” solar term  
234 (November 7–8), the average temperature continuously dropped to below 0 °C, and a thin ice  
235 layer gradually formed on the surface; after the “Rain Water” solar term (February 18–20),  
236 temperatures increased, and the frozen soil began to thaw in both directions; finally, the frozen  
237 soil fully thawed around the “Grain Rain” solar term (April 19–21) in spring (Lyu et al., 2023).  
238 Based on this climatic pattern, we uniformly defined the freezing and thawing periods for all  
239 monitoring wells in the study area. Specifically, the freezing period is defined as the interval  
240 from “Beginning of Winter” to “Rain Water,” and the thawing period as from “Rain Water” to  
241 “Grain Rain.” Therefore, the groundwater level at the “Rain Water” solar term was chosen as  
242 the representative groundwater level during the freezing period to capture the rapid response  
243 of the groundwater level to rising temperatures and thawing of the frozen soil.

244 **2.3. Research methods**

245 **2.3.1. LSTM model**

246 The LSTM neural network (Hochreiter and Schmidhuber, 1997) is an advanced RNN  
247 widely applied in deep learning. It can store and associate previous information, effectively  
248 addressing the issues of vanishing and exploding gradients that occur during the training of  
249 long sequence data. The deep learning model used in this study comprises a single LSTM layer  
250 and a dense layer. The LSTM layer is composed of recurrent cells arranged in a chain-like  
251 structure, allowing information to be passed from the current time step to the next. The model  
252 uses daily precipitation, air temperature, groundwater extraction volume, and snow depth from  
253 the previous 150 days as input sequences to predict groundwater level depths. Each cell in the  
254 LSTM layer includes four components: the input gate ( $i_t$ ), the forget gate ( $f_t$ ), the output gate  
255 ( $o_t$ ), and the cell state ( $c_t$ ) (as shown in the LSTM layer in Fig. 1a). The input gate determines  
256 how much input information is transferred to the cell state. The forget gate primarily controls  
257 how much information from the previous cell state is discarded and how much is carried

258 forward to the current moment. The output gate calculates the output based on the updated cell  
259 state from the forget and input gates. The cell state is used to record the current input, the  
260 previous cell state, and the information from the gate structures. In this study, we adopted the  
261 LSTM equations proposed by Graves et al. (2013), which are represented by the following key  
262 equations:

263  $i_t = \sigma(W_{xi}x_t + W_{hi}h_{t-1} + b_t)$  (1)

264  $f_t = \sigma(W_{xf}x_t + W_{hf}h_{t-1} + b_f)$  (2)

265  $c_t = f_t \odot c_{t-1} + i_t \odot \tanh(W_{xc}x_t + W_{hc}h_{t-1} + b_c)$  (3)

266  $o_t = \sigma(W_{xo}x_t + W_{ho}h_{t-1} + b_o)$  (4)

267  $h_t = o_t \odot \tanh(c_t)$  (5)

268 where the input and output vectors of the implicit layer of the LSTM at time step  $t$  are  $x_t$  and  
269  $h_t$ , respectively, the memory cell is  $c_t$ , and the values of the input, forget, and output gates are  
270  $i_t$ ,  $f_t$ , and  $o_t$ , respectively.  $W$  and  $b$  represent the learnable weight and bias terms to be  
271 estimated during the training period, respectively,  $\sigma(\cdot)$  denotes the logistic sigmoid function,  
272  $\tanh(\cdot)$  is the hyperbolic tangent function, and  $\odot$  represents elementwise multiplication.

273 Before training the model, the air temperature, precipitation, groundwater extraction  
274 volume, and snow depth were normalized by mapping their values to a range between 0 and 1.  
275 The adaptive moment estimation (Adam) algorithm (Kingma and Ba, 2014) was employed  
276 during training, with an initial learning rate set to 0.03. The maximum training epoch number  
277 was configured to 100, and an early stopping strategy was applied to prevent overfitting. For  
278 each individual groundwater monitoring well, 70% of the input–output data pairs were  
279 randomly sampled for training the LSTM model, and they were split into training and  
280 validation samples at a ratio of 7:3. The training samples were repeatedly used to update the  
281 model parameters until the loss function for the validation samples ceased to decrease. The  
282 remaining 30% of the data were used for an independent evaluation of the model performance.

283 Random sampling allows for capturing the overall hydrometeorological variations observed  
284 across different time periods.

285 **2.3.2. Model interpretations**

286 In 2017, Sundararajan et al. developed the integrated gradients (IG) method (Sundararajan  
287 et al., 2017), which uses the gradient of the model's output to the input factors to infer the  
288 specific contribution of the input variables to the output variable. The IG score for an input  
289 factor  $x$  (e.g., the precipitation at the  $i$ -th time step), representing the degree of contribution of  
290 the input variable to the output variable, is expressed as follows:

291 
$$\phi_i^{IG}(f, x, x') = (x_i - x'_i) \int_{\alpha=0}^1 \frac{\partial f(x' + \alpha(x - x'))}{\partial x_i} d\alpha \quad (6)$$

292 where  $\frac{\partial f(x' + \alpha(x - x'))}{\partial x_i}$  denotes the local gradient of the network  $f$  at the interpolation point from  
293 the baseline input ( $x'$ , when  $\alpha = 0$ ) to the target input ( $x$ , when  $\alpha = 1$ ).

294 However, the baseline input  $x'$  in the above formula is a hyperparameter that must be  
295 chosen carefully. In groundwater level studies, if the target input (e.g., a particular groundwater  
296 level observation) is close to the chosen baseline input (e.g., long-term average groundwater  
297 level), i.e.,  $x_i \approx x'_i$ , the IG method may fail to capture the importance of current input factors,  
298 such as precipitation or evaporation, on groundwater level changes (Sturmels et al., 2020). To  
299 address this issue, Jiang et al. (2022) developed the EG method, which is based on the IG  
300 method but assumes that the baseline inputs follow the basic distribution  $D$  sampled from a  
301 background dataset (such as the training dataset), thus avoiding the need to specify a fixed  
302 baseline input. Given the baseline distribution  $D$ , the EG score  $\phi_i^{EG}$  for the  $i$ -th input factor  
303 can be calculated by integrating the gradients over all possible baseline inputs  $x' \in D$ , weighted  
304 by the probability density function  $p_D$ . The EG score represents the influence of input factors  
305 on the model output, with a higher absolute EG score indicating a greater impact of the  
306 corresponding input factor on the model output, while an EG score close to zero suggests that

307 the input factor has little effect on the output. The EG score can be expressed as follows:

308 
$$\phi_i^{EG}(f, x) = \int_{x'} (\phi_i^{IG}(f, x, x') \times p_D(x') dx') \quad (7)$$

309 The above expression involves two integrals, which, according to Erion et al. (2021), can  
310 both be considered expectations. Thus, the equation can be reformulated as:

311 
$$\phi_i^{EG}(f, x) = E_{x' \sim D, \alpha \sim U(0,1)} \left[ (x_i - x'_i) \int_{\alpha=0}^1 \frac{\partial f(x' + \alpha(x-x'))}{\partial x'_i} \right] \quad (8)$$

312 **2.3.3. Evaluation metrics**

313 The evaluation metrics used in this study include the Nash–Sutcliffe efficiency (NSE)  
314 coefficient and the root-mean-square error (RMSE). The NSE is used to assess the degree of  
315 fit of the regression model. The RMSE quantifies how well the predicted values match the  
316 observed values. If the NSE is close to 1 and the RMSE is close to 0, the model is more reliable.

317 
$$NSE = 1 - \frac{\sum_{i=1}^n (x_i - y_i)^2}{\sum_{i=1}^n (x_i - \bar{x}_i)^2} \quad (9)$$

318 
$$RMSE = \sqrt{\frac{\sum_{i=1}^n (x_i - y_i)^2}{n}} \quad (10)$$

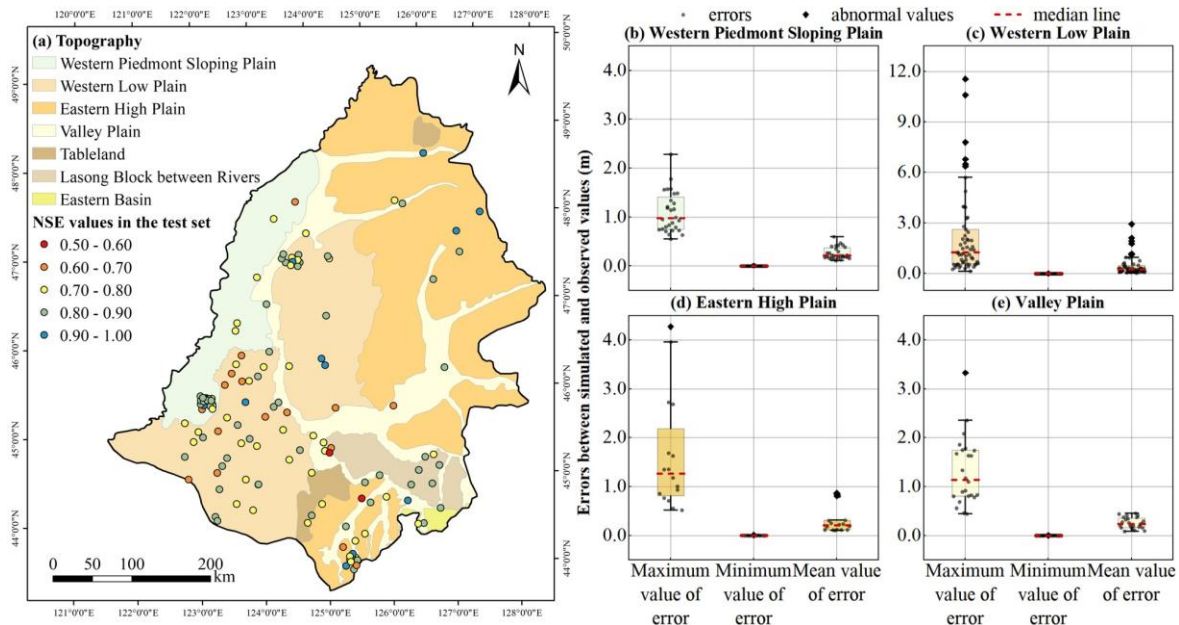
319 where  $x_i$  is the depth of the observed groundwater level, and  $\bar{x}_i$  is the average value of  $x_i$ ;  
320  $y_i$  is the groundwater level depth simulated by the LSTM model; and  $i$  denotes the specific  
321 sample ordinal number, from 1 to  $n$ .

322 **3. Results**

323 **3.1. Simulation Accuracy of Deep Learning Model for Groundwater Level**

324 A data-driven model (LSTM model) was used to simulate the daily groundwater level  
325 depth of 138 aquifer monitoring wells in the Songnen Plain, China, from 2019 to 2021. Overall,  
326 the simulation accuracy of the groundwater level depth was relatively high across the western  
327 piedmont sloping plain, the eastern high plain, and the valley plain regions. In these areas, the  
328 NSE values at the monitoring points in the test set ranged from 0.53 to 0.96 (Fig. 3a), with  
329 87.14% of the monitoring points showing NSE values greater than 0.7. Over the entire

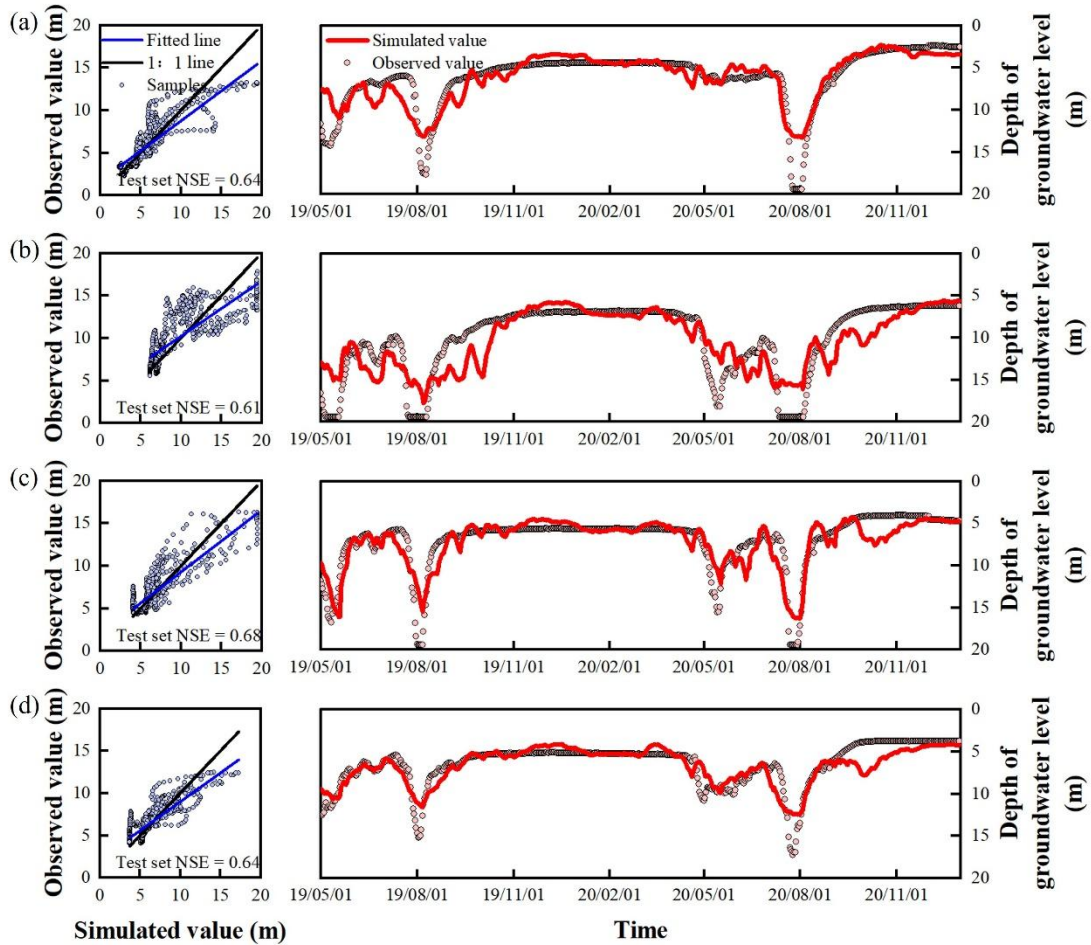
330 simulation period (including the training and test sets), the maximum error between the  
 331 simulated and observed values at each monitoring point mainly ranged from 0.5 to 2.5 m (Fig.  
 332 3b, d, and e), with 94.29% of the monitoring points having an average error of less than 0.5 m.  
 333 The annual groundwater level fluctuation at the monitoring points in this region was relatively  
 334 small, ranging from 0.41 to 6.54 m.



335 **Fig. 3.** (a) Spatial distribution of the NSE values on the test set for 138 groundwater level  
 336 monitoring points in the Songnen Plain, China. (b)–(e) Maximum, minimum, and mean errors  
 337 between simulated and observed groundwater levels at monitoring points in the western  
 338 piedmont sloping plain, western low plain, eastern high plain, and valley plain during the  
 339 simulation period.

341 Only 18.11% of the monitoring wells in the study area had a Nash-Sutcliffe Efficiency  
 342 (NSE) below 0.7 on the test dataset, and these wells were primarily located in the southern part  
 343 of the western low plain (Fig. 3a). In this region, the average absolute error between simulated  
 344 and observed daily groundwater level depth ranged from 0.04 to 2.93 meters, although the  
 345 maximum error reached as high as 11.56 meters (Fig. 3c), indicating that the model exhibited  
 346 certain instability in localized areas. Figure 4 compares the simulated and observed

347 groundwater level depth series at several poorly performing wells in this region. As shown in  
348 the figure, significant discrepancies occurred during certain periods, and the fitting  
349 performance was unsatisfactory. The primary reason for this discrepancy is the large annual  
350 fluctuation in groundwater level depth at many wells in this region: 21.43% of the monitoring  
351 wells had a fluctuation range exceeding 10 meters. These extreme fluctuations posed  
352 challenges for the LSTM model's simulation accuracy. In the training data used for the LSTM  
353 model, samples with extreme values of groundwater level depth were relatively scarce, while  
354 samples with moderate values were more abundant. Consequently, the model tended to fit the  
355 data in the moderate range more accurately, resulting in limited predictive ability for the  
356 extreme ends of the groundwater level series. Despite the reduced accuracy at certain wells,  
357 the LSTM model is capable of accurately capturing the variation trend of groundwater levels,  
358 and no significant lag is observed between the simulated and observed values (Fig. 4). The  
359 Pearson correlation coefficients between the simulated water levels and the measured water  
360 levels at the four representative monitoring points shown in the figure are 0.86, 0.81, 0.87, and  
361 0.85, respectively. Moreover, the correlation coefficients reach their maximum values without  
362 applying any time lag, indicating that the simulated values can effectively and promptly reflect  
363 the actual variation trend of groundwater levels.



364

365 **Fig. 4.** Comparison of the simulated and observed groundwater level depths at typical points  
 366 in the western low plain (NSE values on the test set  $< 0.7$ ).

367 Overall, most of the groundwater monitoring points in the Songnen Plain, China, showed  
 368 NSE values greater than 0.7 on the test set, indicating a relatively high simulation accuracy of  
 369 the groundwater level depth based on the LSTM model. This suggests that the network  
 370 structure of the LSTM model could accurately capture the dynamic relationships between the  
 371 air temperature, precipitation, extraction volume, snow depth, and groundwater level.

372 **3.2. Dynamic Characteristics of Regional Groundwater Level and their Distribution Laws**

373 **3.2.1. Annual Dynamics Variations and Spatial Distribution**

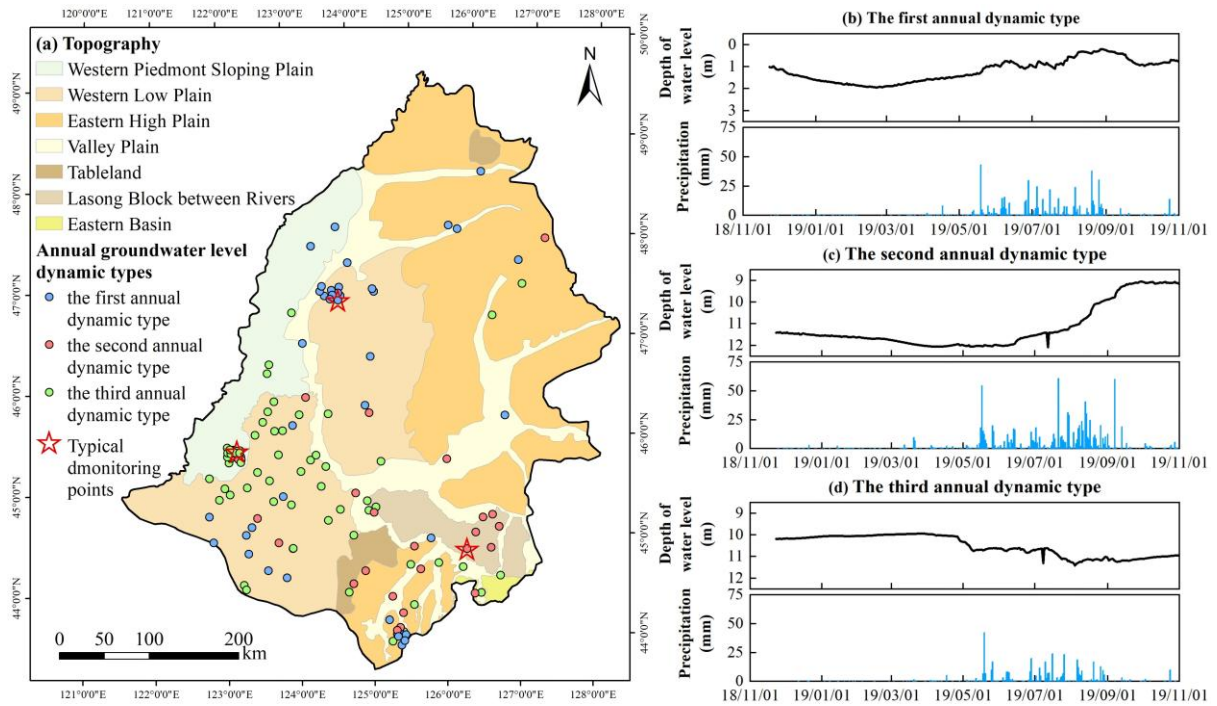
374 Based on the characteristics of the annual groundwater level dynamic curves in the  
 375 Songnen Plain, China, the annual groundwater level dynamics can be categorized into three  
 376 types (Fig. 5).

377        The monitoring wells located in areas with a shallow groundwater level (less than 7 m) in  
378        the northern part of the western low plain and valley plain (Fig. 5a) exhibited annual  
379        groundwater level fluctuations of less than 4 m. Typically, the dynamic change in the  
380        groundwater level is as follows: during the dry season from January to April, precipitation is  
381        almost zero, and the groundwater level depth is significantly greater compared with those in  
382        the other months; with the onset of the rainy season (May to August), precipitation increases,  
383        causing the groundwater level to rise; after the rainy season ends (September to December),  
384        the groundwater level depth gradually increases with decreasing precipitation (Fig. 5b). This  
385        dynamic type of the groundwater level is the first annual dynamic type in the Songnen Plain,  
386        with its corresponding monitoring wells accounting for 29.0% of all wells in the study area.

387        The monitoring wells located on Tableland, the Lasong Block between rivers, and the  
388        eastern high plain (Fig. 5a) have relatively greater groundwater level depths, ranging from  
389        approximately 5 to 11 m. From January to May each year, groundwater levels show a  
390        continuous decline; with the increase in precipitation, the groundwater level begins to gradually  
391        rise, reaching their annual peak in early October (Fig. 5c). The timing of the groundwater peak  
392        is delayed by 1 to 2 months compared with the first dynamic type, indicating that the response  
393        of the groundwater level to precipitation is slower (Fig. 5b and c). The annual groundwater  
394        level fluctuation is within 5 m. This dynamic type is the second annual dynamic type in the  
395        Songnen Plain, with its corresponding monitoring wells accounting for only 18.1% of all wells  
396        in the study area.

397        In agricultural irrigation areas, such as the southern part of the western low plain and the  
398        western piedmont sloping plain (Fig. 5a), the groundwater level depth typically ranges from 5  
399        to 20 m. The dynamic curves of the groundwater level in the aquifer monitoring wells in these  
400        areas exhibit distinct periodicity, showing a funnel-like and sawtooth pattern. The lowest  
401        groundwater levels typically occur in May or August, while the highest level typically occurs

402 in November or later (Fig. 5d). During the irrigation season, groundwater levels drop  
 403 significantly, with annual fluctuations being generally within 15 m. This dynamic groundwater  
 404 type is widely distributed in the study area, with its corresponding monitoring wells accounting  
 405 for 52.9% of all wells, representing the third annual dynamic type in the Songnen Plain.



406  
 407 **Fig. 5.** (a) Spatial distribution of different annual groundwater level dynamic types in the  
 408 Songnen Plain, China; (b–d) Dynamic curves of different annual groundwater types and their  
 409 corresponding precipitation variations. (b) The first annual dynamic type is represented by an  
 410 unconfined aquifer monitoring well, numbered 230204210070, located in the western low plain;  
 411 (c) The second annual dynamic type is represented by an unconfined aquifer monitoring well,  
 412 numbered 220182210411, located in the Lasong Block between rivers; (d) The third annual  
 413 dynamic type is represented by an unconfined aquifer monitoring well, numbered  
 414 220802210145, located in the western piedmont sloping plain.

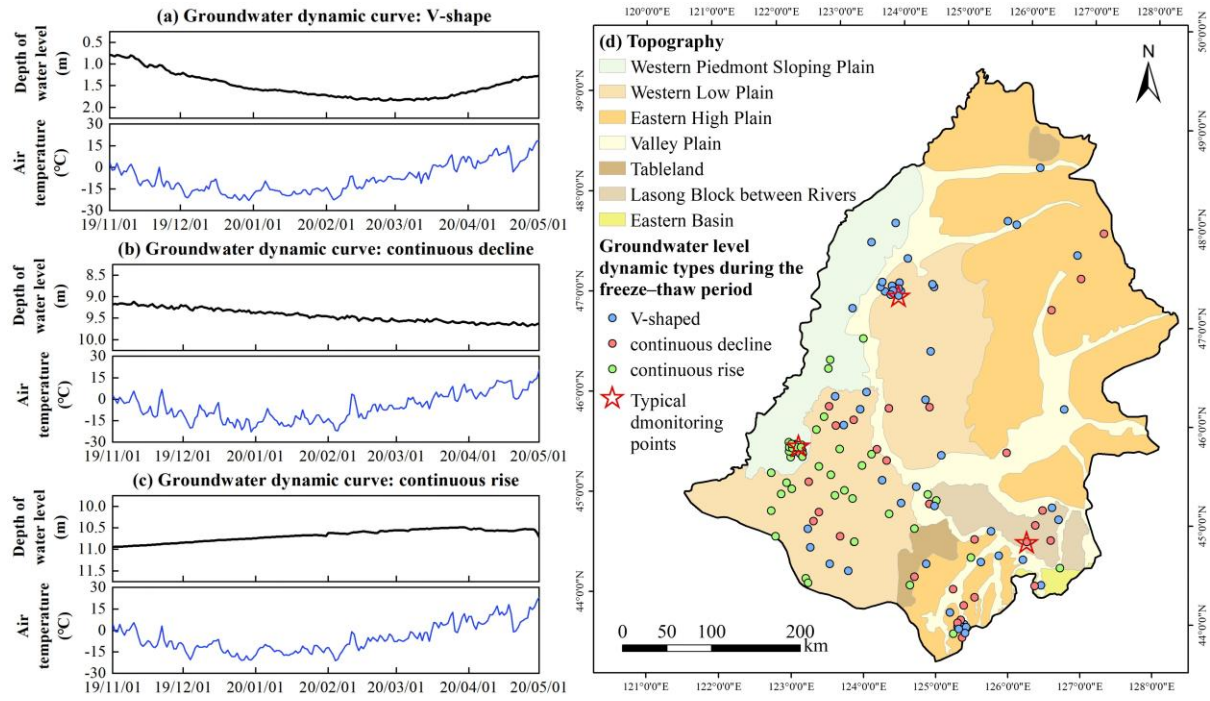
### 415 3.2.2. Freeze–Thaw Period Dynamics Variations and Spatial Distribution

416 Freeze–thaw processes increase the frequency of interactions between soil water and  
 417 groundwater (Daniel and Staricka, 2000; Lyu et al., 2022; Miao et al., 2017). As a typical

418 seasonally frozen soil region, the Songnen Plain, China, exhibits three main forms of the  
419 dynamic curves of the groundwater level during the freeze–thaw period: “decline during  
420 freezing, rise during thawing,” “continuous decline,” and “continuous rise” (Fig. 6). The  
421 monitoring points of the different dynamic types during the freeze–thaw period accounted for  
422 38.4% (V-shaped), 23.2% (continuous decline type) and 38.4% (continuous rise type),  
423 respectively.

424 At monitoring points with a “V-shaped” groundwater level dynamic curve, characterized  
425 by “decline during freezing, rise during thawing” (Fig. 6a), the groundwater level fluctuated  
426 by approximately 0.2–0.9 m during the freeze–thaw period. The time when the groundwater  
427 level reached its maximum depth roughly coincided with the time when the soil reached its  
428 maximum frozen thickness. These monitoring wells are primarily distributed in areas with a  
429 shallow groundwater level in the northern part of the western low plain and the valley plain,  
430 with a few located in the southern part of the western low plain. At the beginning of the freezing  
431 period, groundwater level depths at these wells were typically within 5 m (Fig. 6d).

432 For the continuous decline and continuous rise types, the dynamic curves of the  
433 groundwater level during the freeze–thaw period exhibited either a “continuous decline” or  
434 “continuous rise” (Fig. 6b and c), with the rate of change remaining consistent throughout both  
435 the freezing and thawing periods. Monitoring points with the continuous decline in the  
436 groundwater level were mainly distributed in areas, such as the eastern high plain and the  
437 Lasong Block between rivers, where the groundwater level depth ranged from 4.52 to 11.51 m  
438 at the start of the freezing period (Fig. 6d). In contrast, monitoring wells with a continuous rise  
439 in the groundwater level during the freeze–thaw period were mainly found in agricultural  
440 irrigation areas such as the southern part of the western low plain and the western piedmont  
441 sloping plain, where the groundwater level depth at the beginning of the freezing period ranged  
442 from 4.71 to 19.91 m (Fig. 6d).

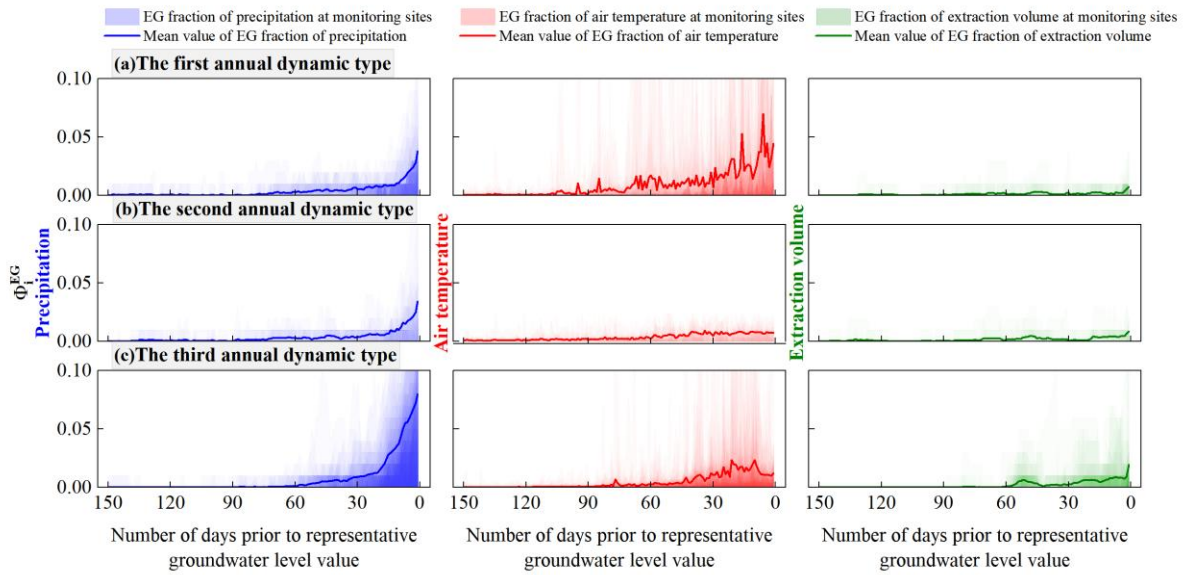


443

444 **Fig. 6.** (a–c) Dynamic curves of different groundwater types during the freeze–thaw period and  
 445 corresponding changes in air temperature; (d) Spatial distribution of different groundwater  
 446 level dynamic types during the freeze–thaw period in the Songnen Plain, China. The dynamic  
 447 curves of the groundwater level exhibiting patterns of (a) V-shaped, (b) continuous decline, and  
 448 (c) continuous rise correspond to the unconfined aquifer monitoring wells numbered  
 449 230204210070, 220182210411, and 220802210145, respectively.

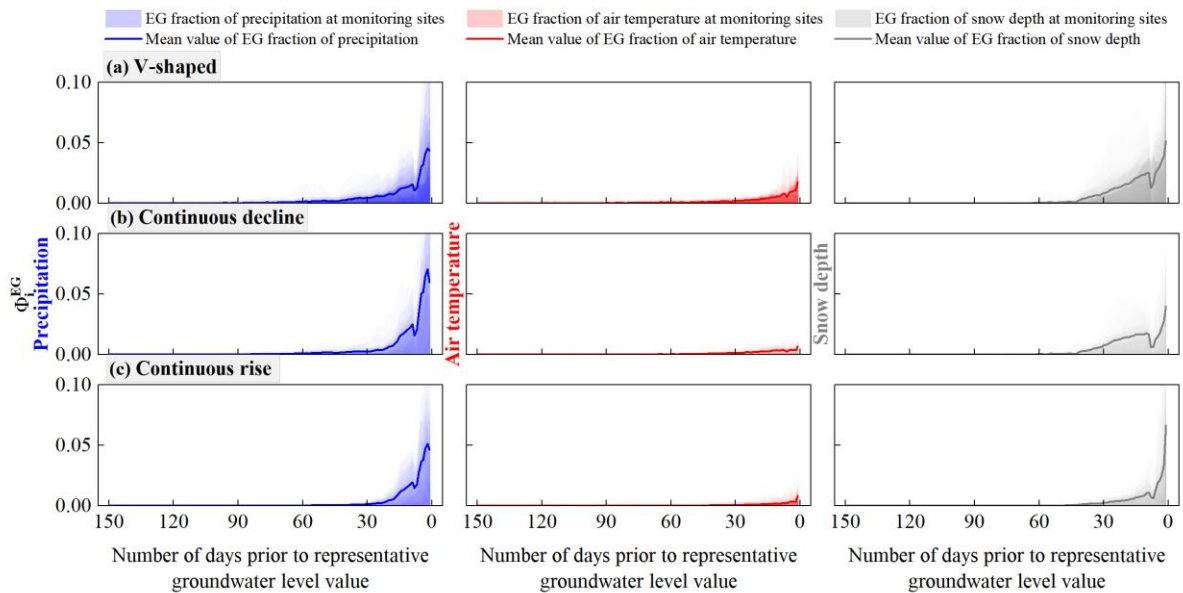
450 **3.3. Main Controlling Factors and Identification of Causes for Various Groundwater Level  
 451 Dynamic Types**

452 After the application of the EG method to the trained models for the 138 groundwater  
 453 level simulations, the EG scores ( $\phi_i^{EG}$ ) were obtained for precipitation, air temperature,  
 454 extraction volume, and snow depth within 150 days prior to the representative groundwater  
 455 level values for each annual and freeze–thaw period groundwater level dynamic type (Figs. 7  
 456 and 8).



457

458 **Fig. 7.** EG scores ( $\phi_i^{EG}$ ) of the precipitation, air temperature, and extraction volume for  
459 different annual groundwater level dynamic types in the study area at different time steps.



460

461 **Fig. 8.** EG scores ( $\phi_i^{EG}$ ) of the precipitation, air temperature, and snow depth for different  
462 groundwater level dynamic types during the freeze–thaw period in the study area at different  
463 time steps.

### 464 3.3.1. Annual Dynamics: Influencing Factors and Dynamics Mechanisms

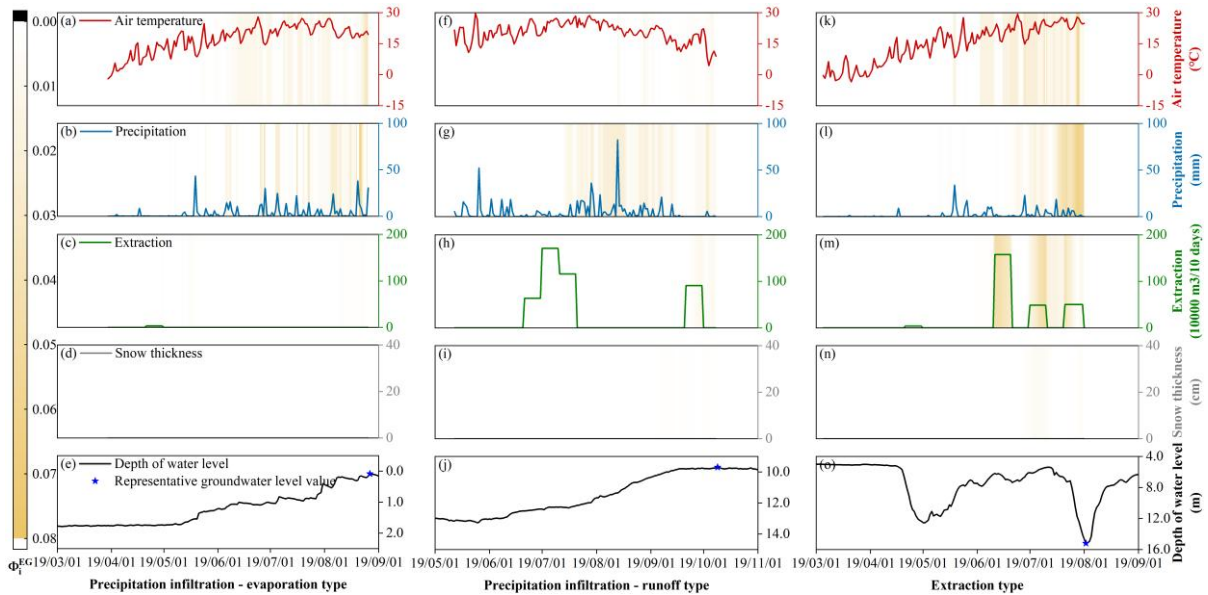
465 Within 90 days before the representative groundwater level values, the average EG scores  
466 for the precipitation and air temperature in the first annual dynamic type ranged from 0 to 0.04

467 and from 0 to 0.07, respectively, while the average EG score for the extraction volume did not  
468 exceed 0.01 (Fig. 7a). This indicates that the groundwater level depth in this dynamic type was  
469 significantly influenced by precipitation and air temperature, while the effect of extraction was  
470 negligible. Thus, the changes in the groundwater level depth may be related to the precipitation  
471 infiltration–evaporation process. When a pronounced precipitation peak occurred (Fig. 9b), the  
472 EG score increased significantly (exceeding 0.15), corresponding to a rise in groundwater level  
473 (Fig. 9e), indicating that precipitation infiltration made a substantial contribution to the  
474 groundwater level increase. Within the 90 days when precipitation influenced the  
475 representative groundwater level value, a total precipitation of 408.09 mm led to an overall rise  
476 in the groundwater level by 1.12 m (Fig. 9b and e). During periods without precipitation, the  
477 air temperature continued to rise (Fig. 9a), reflecting higher soil evaporation. At this time, the  
478 EG score for the air temperature was also relatively high (ranging from 0.10 to 0.20), and the  
479 groundwater level showed a slight decline (Fig. 9e). This suggests that evaporation was the  
480 primary discharge mechanism for groundwater in this dynamic type. Therefore, based on the  
481 groundwater recharge and discharge mechanisms, the first annual groundwater dynamic type  
482 is summarized as the precipitation infiltration–evaporation type.

483 In contrast, in the second annual dynamic type, only the precipitation had a significant  
484 impact on the groundwater level depth within 90 days before the representative groundwater  
485 level value (with the EG scores ranging from 0 to 0.03), while the average EG scores for the  
486 air temperature and extraction volume remained between 0 and 0.01 (Fig. 7b). Precipitation  
487 almost consistently recharged the groundwater during the 90 days before the representative  
488 groundwater level values (with an average EG score of approximately 0.012), causing a gradual  
489 rise in the groundwater level (Fig. 9j). However, the rate of groundwater rise was relatively  
490 slow, with an average value of approximately 0.02 m/d. The air temperature fluctuated  
491 significantly over the 90-day period (Fig. 9f), ranging from 4.41 to 28.57 °C, but had no

492 significant impact on the groundwater level (Fig. 9j). The EG score during periods of high  
493 temperatures was also below 0.01, indicating that evaporation had little effect on the  
494 groundwater level. There was some groundwater extraction in local areas around July and  
495 October (Fig. 9h); however, it had a minimal impact on the groundwater level, with the EG  
496 scores remaining below 0.01. The relatively deep groundwater level (nearly 13 m) suggests  
497 that this groundwater type was primarily discharged through runoff. Therefore, the second  
498 annual groundwater dynamic type was classified as the precipitation infiltration–runoff type.

499 In the third annual dynamic type, the precipitation, air temperature, and extraction volume  
500 had a significant impact on groundwater level within a shorter period before the representative  
501 groundwater level values (within 60 days), with the average EG scores in the ranges of 0–0.08,  
502 0–0.02, and 0–0.02, respectively (Fig. 7c). This dynamic type is mainly distributed in  
503 agricultural irrigation areas, such as the southern part of the western low plain and the western  
504 piedmont sloping plain (Fig. 5a). The main crops in these areas are rice, soybeans, and corn  
505 (You et al., 2021), and their water demand is concentrated in the summer, particularly between  
506 June and August (Xing et al., 2022). During this period, the air temperature shows a fluctuating  
507 uptrend (Fig. 9k), with the EG scores reaching a maximum of 0.02, indicating that high  
508 temperatures increase soil evaporation and crop transpiration. This leads to a higher water  
509 demand from the crops; however, the low rainfall was insufficient to meet this demand during  
510 these periods (Fig. 9l, with a daily maximum precipitation of only 33.80 mm), necessitating  
511 additional groundwater extraction for irrigation to maintain crop growth (Fig. 9m). As a result,  
512 the EG score for the extraction volume reached approximately 0.20 during this period, and  
513 groundwater level decreased accordingly (Fig. 9o). This dynamic type indicates that  
514 groundwater recharge comes from precipitation infiltration, and groundwater extraction is the  
515 main discharge mechanism. Thus, the third annual groundwater dynamic type was classified  
516 as the extraction type.



517

518 **Fig. 9.** Observed values and EG scores ( $\phi_i^{EG}$ ) of the precipitation, air temperature, extraction  
 519 volume, and snow depth within 150 days before the representative groundwater level values  
 520 for various annual groundwater level dynamic types, as well as the corresponding annual  
 521 groundwater level depth dynamic curves. The precipitation infiltration–evaporation type,  
 522 precipitation infiltration–runoff type, and extraction type are represented by monitoring wells  
 523 230204210072, 220183210399, and 220821210024, with representative groundwater level  
 524 values corresponding to August 27, 2019, October 9, 2019, and August 2, 2019, respectively.

525 **3.3.2. Freeze–Thaw Dynamics: Influencing Factors and Dynamics Mechanisms**

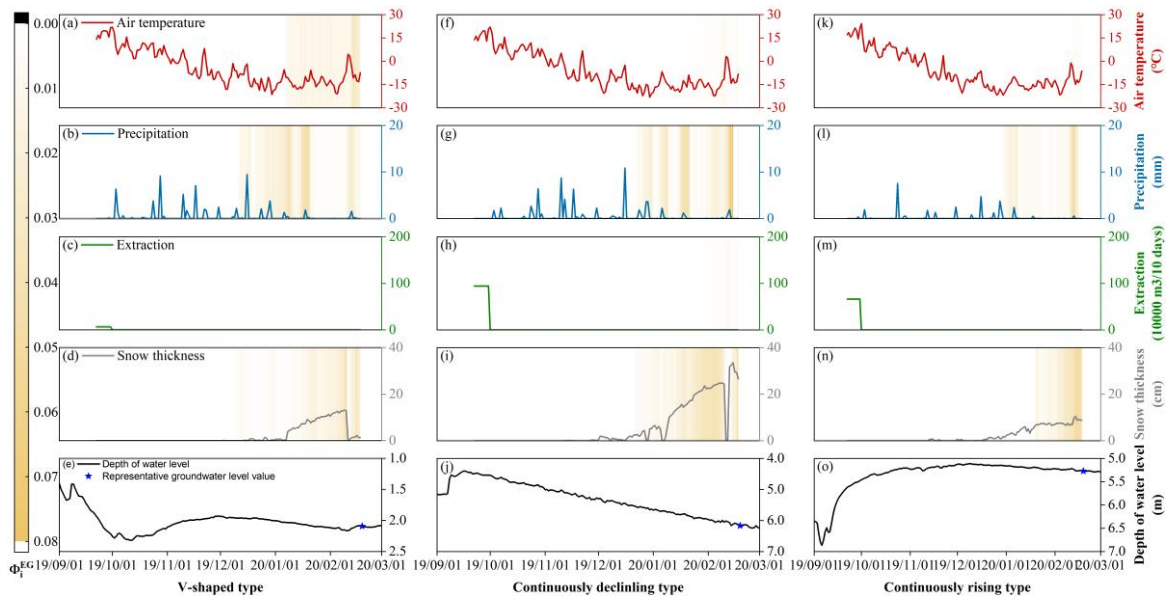
526 A further analysis focused on the groundwater dynamic types during the freeze–thaw  
 527 period. In the V-shaped dynamic type, the average EG scores for precipitation and snow depth  
 528 within 60 days before the representative groundwater level values ranged from 0 to 0.05, while  
 529 the average EG score for the air temperature within 30 days before the representative  
 530 groundwater level values ranged from 0 to 0.02 (Fig. 8a). This suggests that the air temperature,  
 531 precipitation, and snow depth had a combined effect on the groundwater level depth of the V-  
 532 shaped dynamic type during the freeze–thaw period. Within 30 days before the representative  
 533 groundwater level values, the air temperature ranged from  $-21.10^{\circ}\text{C}$  to  $4.40^{\circ}\text{C}$ , with the  
 534 overall temperature being below  $0^{\circ}\text{C}$  (Fig. 10b). As the air and soil temperatures dropped

535 below 0 °C, the effective soil porosity decreased significantly due to water freezing, and the  
536 low-temperature suction related to the soil water potential between ice and water in the frozen  
537 soil increased gradually (Lyu et al., 2022). Under the combined effect of the capillary force and  
538 low-temperature suction, groundwater migrated upward continuously, thereby increasing the  
539 groundwater level depth (Fig. 10e). During this period, the snow depth increased with the  
540 decrease in temperature, reaching a maximum value of 13.22 cm on February 9, 2020 (Fig.  
541 10d). The maximum EG score for the snow depth reached 0.03, indicating that snow had an  
542 impact on the groundwater level depth during the freeze–thaw period. When the air temperature  
543 exceeded 0 °C, the snow thawed rapidly (Fig. 10d), and the snow and frozen soil thaw water  
544 infiltrated to recharge the groundwater, causing the groundwater level to rise for the first time  
545 (Fig. 10e).

546 For the continuously declining and continuously rising dynamic types, only precipitation  
547 and snow depth affected the groundwater level depth during the freeze–thaw period. In the  
548 continuously declining groundwater dynamic type, the precipitation and snow depth influenced  
549 the groundwater level depth over a longer period before the representative groundwater level  
550 values (within 60 days), with the average EG scores below 0.07 and 0.04, respectively (Fig.  
551 8b). In the continuously rising groundwater dynamic type, the average EG scores for the  
552 precipitation and snow depth within 30 days before the representative groundwater level values  
553 ranged from 0 to 0.05 and from 0 to 0.07, respectively, indicating that precipitation and snow  
554 depth affected the groundwater level depth in this dynamic type during the freeze–thaw period  
555 (Fig. 8c). Compared with precipitation and snow depth, the impact of the air temperature on  
556 the groundwater level in both dynamic types was negligible (Fig. 8b and c), with the average  
557 EG scores ranging from 0 to 0.01.

558 In both the freeze–thaw dynamic types, the air temperature fluctuated significantly over  
559 the past 150 days (Fig. 10f and k), whereas the EG scores remained below 0.01, indicating that

560 the freeze–thaw effects had no significant impact on groundwater levels. Snow depth continued  
 561 to increase during the winter when the air temperature was below 0 °C (Fig. 10i and n). When  
 562 the air temperature rose above 0 °C, the snow gradually thawed, and the meltwater had some  
 563 recharging effect on groundwater levels (with maximum EG scores reaching 0.04). However,  
 564 due to the limited amount of snow and the high groundwater levels, the impact of snowmelt on  
 565 the groundwater level was gradual and limited, failing to significantly alter the original trends  
 566 in the continuously declining or continuously rising groundwater levels (Fig. 10j and o).  
 567 Therefore, the causes of the continuously declining and continuously rising groundwater level  
 568 dynamic types were related to the recovery process of the annual groundwater levels.



569  
 570 **Fig. 10.** Observed values and EG scores ( $\phi_i^{EG}$ ) of the precipitation, air temperature, extraction  
 571 volume, and snow depth within 150 days before the representative groundwater level values  
 572 for various groundwater level dynamic types during the freeze–thaw period, as well as the  
 573 corresponding annual groundwater level depth dynamic curves. The V-shaped, continuous  
 574 decline, and continuous rise types are represented by monitoring wells 220106210371,  
 575 220182210410, and 220821210024, respectively. The representative groundwater level  
 576 corresponds to February 19, 2020.

577 **3.4. Regional Distribution Characteristics of the Dynamic Causes of Groundwater Level in**

578 ***the Songnen Plain, China***

579 Based on the dynamic variations and spatial distribution characteristics of the groundwater  
580 levels in the study area, groundwater monitoring points where the groundwater levels dropped  
581 in the freezing period and rose in the thawing period, driven by soil freeze–thaw processes,  
582 typically showed a precipitation infiltration–evaporation dynamic in terms of the groundwater  
583 level dynamics during the year (Figs. 5b and 6a). These points were mainly distributed in areas  
584 with shallow groundwater level depths, such as the northern part of the western low plain and  
585 valley plain (Figs. 11a and 12a). Groundwater level dynamics unaffected by soil freeze–thaw  
586 processes generally showed two trends: continuous decline or continuous rise (Fig. 6b and c).  
587 Monitoring points with a continuous decline trend were mainly located in areas with a  
588 significant groundwater level depth, such as the eastern high plain and the Lasong Block  
589 between the rivers, where the annual groundwater level dynamics showed typical dynamic  
590 characteristics of precipitation infiltration–runoff type (Fig. 5c). The monitoring points in  
591 agricultural irrigation areas in the southern part of the western low plain and the western  
592 piedmont sloping plain showed a continuous rise in the groundwater level during the freeze–  
593 thaw period (Fig. 12a), and the dynamic type of the groundwater level in the year was mainly  
594 the extraction type (Fig. 5d). Therefore, the “continuous decline” groundwater dynamic during  
595 the freeze–thaw period was the recession phase of the groundwater level after the flood season  
596 peak in the precipitation infiltration–runoff-type groundwater, while the “continuous rise”  
597 groundwater dynamic was the recovery phase of the groundwater level after the extraction in  
598 the extraction-type groundwater.

599 However, under the classification based on the freeze–thaw period, the proportions of the  
600 V-shaped, continuous decline, and continuous rise types accounted for 38.4%, 23.2%, and 38.4%  
601 of all monitoring points, respectively. These proportions did not completely align with the  
602 annual classification of the precipitation infiltration–evaporation (29.0%), precipitation

603 infiltration–runoff (18.1%), and extraction (52.9%) types. This discrepancy can be partly  
604 attributed to differences in the groundwater level depth. In some extraction monitoring points,  
605 although the annual groundwater level dynamics showed typical extraction characteristics,  
606 because the groundwater level at these monitoring points was shallow, the soil freezing and  
607 thawing processes still had a significant impact on it, resulting in a V-shape water level change  
608 at these points during the freeze–thaw period. The presence of such monitoring points increased  
609 the proportion of the V-shape type during the freeze–thaw period, while reducing the proportion  
610 of the continuous-rise type. Thus, the proportions of the freeze–thaw and annual classifications  
611 were not entirely consistent, particularly in areas with a shallow groundwater level depth,  
612 where soil freezing and thawing caused groundwater levels at some points of the extraction  
613 type to exhibit V-shaped variations during the freeze–thaw period.

614 In the northern part of the western low plain, where groundwater level was shallow (less  
615 than 5 m), the predominant annual groundwater dynamic was the precipitation infiltration–  
616 evaporation type (Fig. 11a). Due to the proximity of the groundwater level to the surface, the  
617 groundwater levels in these areas are more sensitive to meteorological factors. The dynamic  
618 curves of the groundwater level show a characteristic in that the high water level period  
619 corresponds to the rainy season. Specifically, in the Songnen Plain, peak precipitation and  
620 groundwater level in this dynamic type occur simultaneously, typically between July and  
621 August (Fig. 11d and f). The annual variation in the groundwater level was small, generally  
622 less than 4 m (Fig. 11c). During the freeze–thaw period, the groundwater level dynamics in this  
623 type exhibited a V-shaped pattern, with the groundwater level declining during the freezing  
624 period and rising during the thawing period, with a fluctuation range of 0.2–0.9 m. However,  
625 this V-shaped variation in the groundwater level is not accidental. At monitoring points with V-  
626 shaped dynamics, the initial groundwater level depth and soil freezing depth at the beginning  
627 of the freezing period were in the ranges of 0–5 m (Fig. 12d) and 1.6–2.1 m (Fig. 12c),

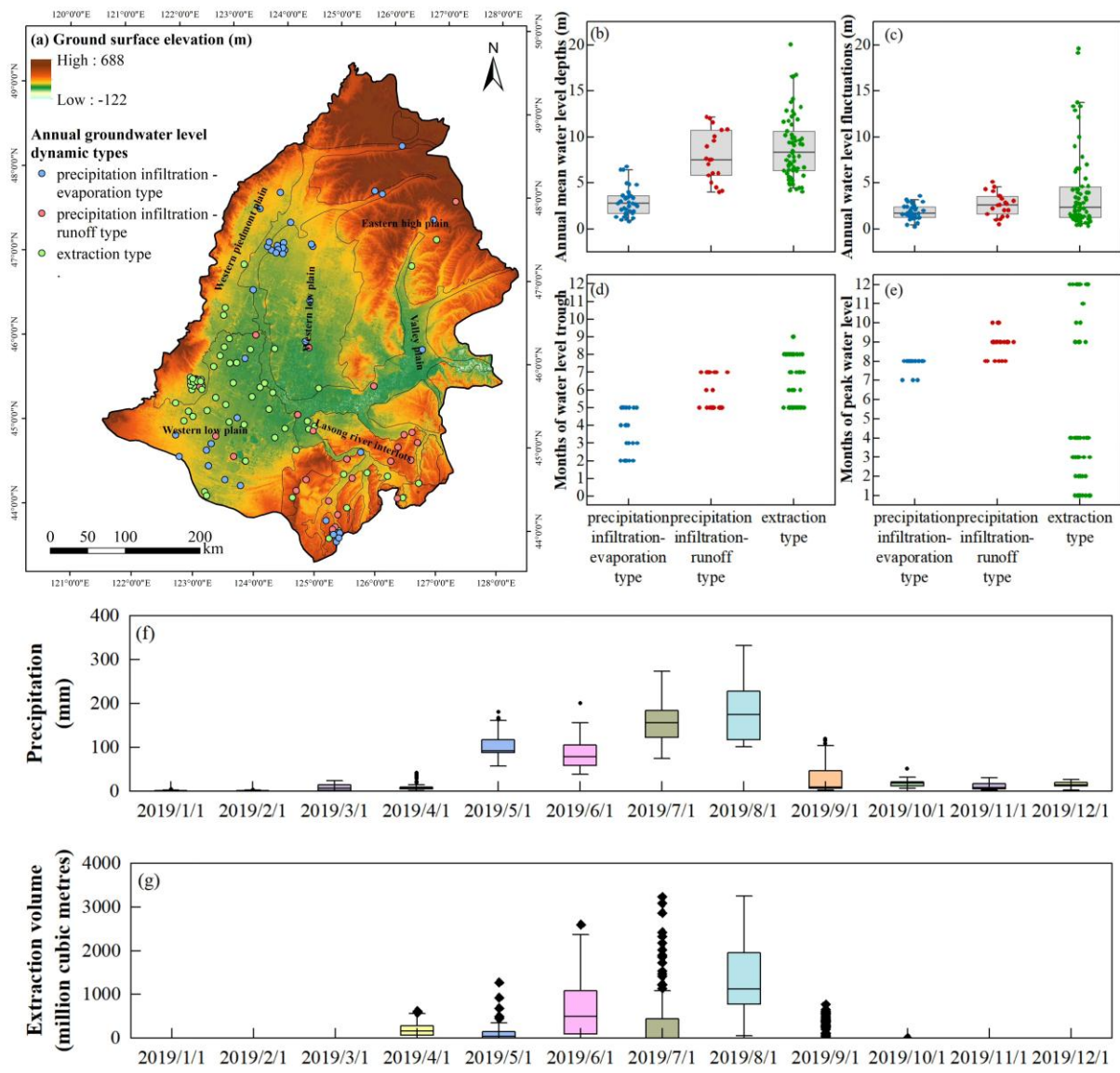
628 respectively. The soil was predominantly silty clay, with a maximum capillary rise height of up  
629 to 5 m (Rui, 2004). Therefore, the initial groundwater level depth at these points was generally  
630 less than the sum of the soil freezing depth and the maximum capillary rise height (Fig. 12a).  
631 This means that during the freezing period, the low-temperature suction caused by soil freezing  
632 and the pre-existing capillary forces in the soil form a complete hydraulic connection between  
633 the frozen layer and the groundwater, causing the groundwater to continuously migrate toward  
634 the freezing front during the freezing period.

635 Groundwater monitoring points exhibiting the precipitation infiltration-runoff type were  
636 mainly distributed in the eastern high plain and the Lasong Block between rivers. In these areas,  
637 the groundwater level is deeper, typically ranging from 5 to 12 m (Fig. 11b), and runoff is the  
638 primary mode of groundwater discharge. The deeper groundwater level prolongs the infiltration  
639 time of precipitation, resulting in a delayed response of the groundwater level dynamics to  
640 precipitation recharge. Groundwater level peaks typically occur between August and October  
641 (Fig. 11d), lagging behind the precipitation peak by approximately one month (Fig. 11f). Due  
642 to the low recharge rate, groundwater level fluctuations are relatively moderate, with annual  
643 variations generally within 4 m (Fig. 11c). During the freeze-thaw period, groundwater  
644 monitoring points with continuously declining trends have greater initial groundwater level  
645 depths, ranging from 4.52 to 11.51 m at the beginning of the freezing period (Fig. 12d). This  
646 feature is primarily caused by the groundwater level rebound following the cessation of  
647 extraction after the irrigation period. With the cessation of agricultural water withdrawal, the  
648 depression cone formed by intensive extraction in the earlier stage begins to be replenished,  
649 and the groundwater level subsequently rises slowly. Due to the previously high extraction  
650 intensity and the relatively deep groundwater table, the recovery process does not occur  
651 instantaneously; instead, it is jointly constrained by the delayed response of the groundwater  
652 system and the regional recharge conditions. As a result, the groundwater level exhibits a steady

653 and sustained upward trend. In addition, the soil freezing depth in this dynamic type was  
654 shallower (between 1.6 and 1.8 m), and the soil was still primarily silty clay (Fig. 12b and c).  
655 The greater groundwater level depth and shallower soil freezing depth prevented a complete  
656 hydraulic connection between the frozen soil and groundwater (Fig. 12a), resulting in the  
657 groundwater level being unaffected by the soil freeze–thaw process. Therefore, under  
658 conditions where no groundwater extraction occurs during the freeze–thaw period and the  
659 groundwater level is not influenced by freeze–thaw processes, the groundwater system  
660 continues the post-irrigation recovery process, presenting a “sustained rising” groundwater  
661 level pattern.

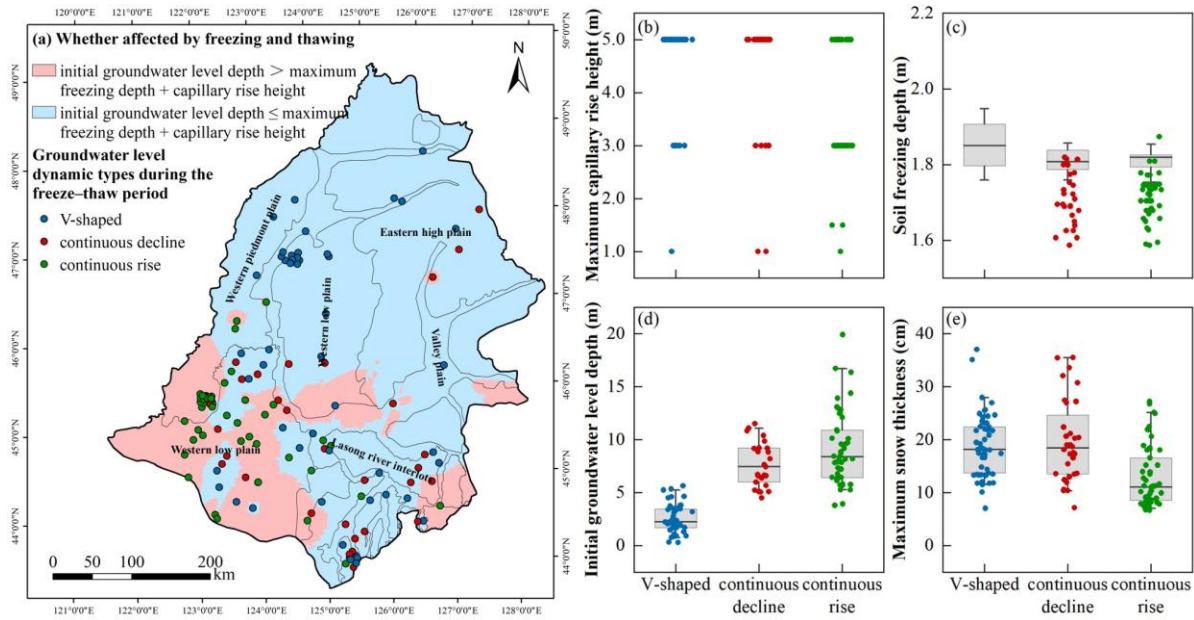
662 In the agricultural irrigation areas of the southern part of the western low plain and the  
663 western piedmont sloping plain, the groundwater level depth corresponding to the extraction  
664 types typically ranged from 5 to 20 m (Fig. 11b). During the agricultural irrigation period,  
665 significant groundwater extraction led to a marked decline in the groundwater level (Fig. 11c).  
666 The low groundwater level period coincided with the peak extraction period, typically between  
667 June and August (Fig. 11e and g). In areas with substantial groundwater extraction, a  
668 groundwater depression cone had already formed, with annual groundwater level fluctuations  
669 reaching up to 15 m (Fig. 11c). During the freeze–thaw period, the groundwater level dynamics  
670 exhibited a continuous rising trend. In the southern part of the western low plain and the  
671 western piedmont sloping plain, the initial groundwater level depth at the beginning of the  
672 freezing period and the soil freezing depth were in the ranges of 5–20 m (Fig. 12d) and 1.6–  
673 1.8 m (Fig. 12c), respectively, with the soil primarily comprising silty clay and sandy clay loam  
674 (with a maximum capillary rise height of 3 m) (Fig. 12b). In this region, the initial groundwater  
675 level depth was generally greater than the sum of the soil freezing depth and the maximum  
676 capillary rise height, causing the hydraulic connection between the vadose and saturated zones  
677 to be severed (Fig. 12a), and the groundwater level was unaffected by the soil freeze–thaw

678 process.



679

680 **Fig. 11.** (a) Spatial distribution of the ground surface elevation and three dynamic types of  
 681 annual groundwater level (precipitation infiltration-evaporation type, precipitation infiltration-  
 682 runoff type, and extraction type) in Songnen Plain, China. The correlation between the three  
 683 dynamic types of annual groundwater level and (b) annual mean groundwater level depths, (c)  
 684 annual water level fluctuations, (d) months of peak water level and (e) months of water level  
 685 trough. (f) and (g) Monthly distribution of the precipitation and extraction volume in Songnen  
 686 Plain, China in 2019, respectively. Each point in (b)–(e) represents a groundwater level  
 687 monitoring point.



688

689 **Fig. 12.** (a) Spatial distribution of whether the groundwater level is affected by the soil freeze–  
690 thaw process and the three groundwater level dynamic types during the freeze–thaw period (V–  
691 shaped, continuously declining, and continuously rising) in the Songnen Plain, China.  
692 Correlations between the groundwater level dynamic types in the three freeze–thaw period and  
693 (b) maximum capillary rise height of the soil, (c) the soil freezing depth, (d) the initial  
694 groundwater level depth at the start of the freezing period, and (e) maximum snow thickness.  
695 Each point in (b)–(e) represents a groundwater monitoring well.

#### 696 4. Discussion

##### 697 4.1. Implications of Groundwater Level Dynamics Classification for Water Resources 698 Management

699 This study identified three main types of annual groundwater level dynamics in the  
700 Songnen Plain: the precipitation infiltration–evaporation type (29.0%), the precipitation  
701 infiltration–runoff type (18.1%), and the extraction type (52.9%). This classification helps to  
702 reveal in greater depth the spatiotemporal distribution characteristics and response patterns of  
703 regional groundwater dynamics. Xu et al. (2024) demonstrated, based on random forest model  
704 analysis, that precipitation is the primary source of recharge for shallow groundwater in the

705 Songnen Plain. This finding is consistent with the identification of the precipitation infiltration–  
706 type groundwater dynamics in this study, supporting the regulatory role of natural processes in  
707 groundwater levels. Meanwhile, Wu et al. (2025) reported that the significant groundwater  
708 decline in Jilin Province is mainly due to over-extraction for agricultural irrigation, particularly  
709 the large water demand associated with extensive rice cultivation. This observation echoes the  
710 finding that the extraction type accounts for the largest proportion of groundwater dynamics in  
711 this study, highlighting the substantial impact of human pumping activities on groundwater  
712 resources. On this basis, differentiated management strategies should be implemented for  
713 different groundwater dynamics types: in areas dominated by natural processes, ecological  
714 water requirements should be safeguarded and precipitation resources should be utilized  
715 comprehensively; in areas with significant human extraction, pumping schemes should be  
716 optimized to prevent ecological and social risks associated with excessive groundwater level  
717 decline.

718 During the freezing–thawing period, groundwater level dynamics are mainly divided into  
719 V-shaped type (38.4%), continuously declining type (23.2%), and continuously rising type  
720 (38.4%), reflecting different response patterns of the groundwater system under the complex  
721 hydrological processes in seasonally frozen soil areas. Previous studies have indicated that soil  
722 freezing and thawing during the freezing–thawing period have significant impacts on  
723 groundwater recharge and discharge processes (e.g., Wang et al., 2023; Xie et al., 2021). The  
724 classification method adopted in this study, by identifying the overall dynamic characteristics  
725 during the freezing–thawing period, provides a more comprehensive description of  
726 groundwater response patterns. This classification not only facilitates accurate delineation of  
727 potential recharge and deficit zones in spring but also provides a theoretical basis for  
728 formulating differentiated water resources management strategies tailored to the freezing–  
729 thawing cycle, thereby enhancing the capacity to regulate groundwater dynamics in seasonally

730 frozen soil areas.

#### 731 ***4.2 A New Perspective on Identifying Groundwater Level Dynamics Mechanisms***

732 Previous studies on the causes of groundwater level dynamics have generally relied on  
733 two main approaches. The first involves statistical methods such as trend analysis, correlation  
734 regression, or principal component analysis combined with the temporal variations of driving  
735 factors like precipitation, temperature, and water usage to infer potential dominant controls  
736 (Sarkhel et al., 2024). The second approach constructs numerical groundwater models or  
737 hydrogeological process-based models that quantify the influence of different drivers through  
738 parameter inversion, based on known aquifer structures, boundary conditions, and recharge-  
739 discharge processes (Petio et al., 2024). However, these methods face significant limitations  
740 when applied at the regional scale: statistical methods struggle to fully characterize complex  
741 nonlinear responses with multiple time lags and scales, while process-based models depend  
742 heavily on high-precision hydrogeological parameters that are often unavailable in most  
743 regions, and their results are susceptible to biases introduced by prior assumptions.

744 Differing from previous groundwater level dynamics research, this study explores the  
745 dominant factors and their mechanisms controlling various groundwater level changes in the  
746 Songnen Plain from the perspective of extracting information embedded within the LSTM  
747 model, thereby achieving a data-driven, bottom-up mechanism identification. This approach  
748 relies solely on multi-source observational data (precipitation, temperature, snow thickness,  
749 groundwater extraction, etc.) and can reveal the spatial (across monitoring wells) and temporal  
750 (intra-annual and seasonally frozen soil periods) patterns of dominant factor effects without  
751 requiring inaccessible hydrogeological data such as aquifer parameters and recharge-discharge  
752 relationships. Compared to traditional process-based models, this method not only enhances  
753 the feasibility and applicability of causative analysis but also reduces biases stemming from  
754 prior assumptions, providing a more realistic reflection of the groundwater system's response

755 mechanisms (Jiang et al., 2022).

756 ***4.3. Limitations of existing models***

757 A deep learning model was successfully developed in this study to simulate the  
758 groundwater level in the seasonally frozen ground regions of Northeast China, with 81.88% of  
759 the monitoring wells in the study area achieving an  $NSE > 0.7$  on the test set. A common issue  
760 with deep learning models is that they are often considered black-box models, making it  
761 difficult to interpret their internal decision-making processes, which limits their credibility and  
762 interpretability in practical applications (Gunning et al., 2019). In groundwater level simulation  
763 studies, this research is the first to apply the EG method to quantify the importance of input  
764 factors in simulating groundwater level during non-freezing and freezing periods, revealing the  
765 driving forces behind groundwater level dynamics in different seasons. The introduction of this  
766 method offers a novel approach to understanding the groundwater level dynamics in seasonally  
767 frozen regions.

768 We opted for a local modeling approach (i.e., training a separate model for each  
769 groundwater monitoring well) rather than a regional approach (training a single model with  
770 data from multiple monitoring wells). This decision was based on our goal to identify the  
771 contribution patterns of the input factors (precipitation, air temperature, extraction volume, and  
772 snow depth) to groundwater level at the regional scale, including the duration of their influence  
773 and the significance of their impact. From a prediction standpoint, a regional model might be  
774 more suitable for areas where data are scarce or incomplete (Frame et al., 2022; Nearing et al.,  
775 2021), as it can learn more general relationships between input and output factors from  
776 historical data (Kratzert et al., 2019). However, regional models are associated with the issue  
777 of multicollinearity between static factors, and this issue must be addressed. Collinear input  
778 factors may share a substantial amount of information, making it difficult for the model to  
779 accurately distinguish the independent influence of each input factor on the output, leading to

780 challenges in interpreting the impact of inputs on the output. Therefore, using regional models  
781 to explain the causes of groundwater level dynamics in seasonally frozen regions could be more  
782 challenging than using local models. Nevertheless, we acknowledge the advantages of regional  
783 models. Future research could further explore how to address the multicollinearity issues  
784 associated with static factors in regional models. In conclusion, we successfully combined deep  
785 learning models with the EG method to reveal the causes of groundwater level dynamics in  
786 seasonally frozen regions.

787 **5. Conclusions**

788 Groundwater dynamics in seasonally frozen regions are complex, influenced by both  
789 climate variability and human activities. Deep learning models require more sophisticated  
790 architectures and broader input variables to improve simulation accuracy, but this increases the  
791 difficulty of interpreting their internal mechanisms. Therefore, this study applies an  
792 interpretable deep learning approach to reveal the driving mechanisms behind groundwater  
793 level dynamics in seasonally frozen soil regions. High-precision simulations of groundwater  
794 levels at 138 monitoring points were conducted using an LSTM model, and combined with the  
795 EG method, the main controlling factors and underlying mechanisms of different types of water  
796 level changes were identified. The main findings are as follows:

797 First, the LSTM model demonstrated high accuracy in simulating groundwater level  
798 variations in seasonally frozen areas, with NSE values on the test set ranging from 0.53 to 0.96,  
799 indicating its effectiveness in capturing complex groundwater dynamics.

800 Second, by applying the EG method, three dominant intra-annual groundwater dynamic  
801 types in the Songnen Plain of China were identified: precipitation infiltration–evaporation type  
802 (29.0%), precipitation infiltration–runoff type (18.1%), and extraction type (52.9%).  
803 Correspondingly, during the freeze–thaw period, these types are reflected as V-shaped,  
804 continuously declining, and continuously rising patterns, accounting for 38.4%, 23.2%, and

805 38.4% of the monitoring wells, respectively.

806 Third, while all three intra-annual types are primarily recharged by precipitation  
807 infiltration, their discharge pathways differ: evaporation, runoff, and groundwater extraction,  
808 respectively. During the freeze–thaw period, changes in the soil water potential gradient due to  
809 freezing and thawing lead to interactions between soil water and groundwater, resulting in the  
810 V-shaped variation. In contrast, the continuously rising and types declining reflect gradual  
811 water level changes primarily driven by groundwater extraction and precipitation recharge,  
812 without strong influence from freeze–thaw processes. These dynamic types represent  
813 groundwater fluctuations jointly driven by multiple factors across different temporal scales.

814 The results demonstrate the great potential of the EG method to bridge model accuracy  
815 and interpretability, offering a new perspective for analyzing complex hydrological processes.  
816 Future research may incorporate more advanced interpretability techniques to further enhance  
817 understanding of deep learning models. The significance of deep learning lies not only in high-  
818 accuracy simulations, but also in advancing the discovery of hydrological mechanisms. This  
819 study provides new methodological support and theoretical insights for groundwater resource  
820 management in seasonally frozen soil regions.

## 821 **Code and data availability**

822 The precipitation and air temperature data were obtained from the ERA5 hourly data on  
823 single levels from 1979 to present dataset, available at  
824 <https://cds.climate.copernicus.eu/datasets/reanalysis-era5-single-levels?tab=download>  
825 (Hersbach et al., 2023). The snow depth data were provided by the National Tibetan Plateau  
826 Data Center, accessible at <http://data.tpdc.ac.cn/> (Che et al., 2015). The surface elevation data  
827 were obtained from the Geospatial Data Cloud (<https://www.gscloud.cn/search>). The  
828 groundwater level data were provided by the China Institute of Geo-Environment Monitoring.  
829 The code for the explainable machine learning framework is available at

830 <https://doi.org/10.5281/zenodo.4686106> (Jiang, 2022).

831 **Credit authorship contribution statement**

832 H.L.: Conceptualization, Investigation, Formal analysis, Data curation, Visualization,  
833 Writing—original draft. H.Ly.: Conceptualization, Validation, Formal analysis, Resources,  
834 Investigation, Data curation, Visualization, Supervision. B.P.: Investigation, Visualization.  
835 X.Su.: Investigation, Supervision. W.D.: Resources, Data curation. Y.W.: Resources, Data  
836 curation. T.S.: Data curation. X.Sh.: Data curation.

837 **Declaration of interests**

838 The authors declare that they have no known competing financial interests or personal  
839 relationships that could have appeared to influence the work reported in this paper.

840 **Disclaimer**

841 Publisher's note: Copernicus Publications remains neutral with regard to jurisdictional  
842 claims in published maps and institutional affiliations.

843 **Acknowledgments**

844 This research was supported by the Jilin Provincial Science and Technology Development  
845 Plan Project (No.20230508036RC) and National Natural Science Foundation of China  
846 (42172267, 42230204, U19A20107). Thanks to Groundwater Monitoring Project of China  
847 Institute of Geo-Environment Monitoring for providing data support.

848 **References**

849 Ao, C., Zeng, W., Wu, L., Qian, L., Srivastava, A. K., and Gaiser, T.: Time-delayed machine  
850 learning models for estimating groundwater depth in the Hetao Irrigation District, China,  
851 Agr. Water Manage., 255, 107032, <https://doi.org/10.1016/j.agwat.2021.107032>, 2021.  
852 Che, T., Dai, L., Li, X.: Long-term series of daily snow depth dataset in China (1979-2024).  
853 National Tibetan Plateau / Third Pole Environment Data Center.  
854 <https://doi.org/10.11888/Geogra.tpdc.270194>, 2015.

855 Daniel, J. A., and Staricka, J. A.: Frozen soil impact on ground water–surface water interaction,  
856 J. Am. Water Resour. Assoc., 36, 151–160, <https://doi.org/10.1111/j.1752-1688.2000.tb04256.x>, 2000.

858 Demissie, Y. K., Valocchi, A. J., Minsker, B. S., and Bailey, B. A.: Integrating a calibrated  
859 groundwater flow model with error-correcting data-driven models to improve predictions,  
860 J. Hydrol., 364, 257–271, <https://doi.org/10.1016/j.jhydrol.2008.11.007>, 2009.

861 Ebrahimi, H., and Rajaee, T.: Simulation of groundwater level variations using wavelet  
862 combined with neural network, linear regression and support vector machine, Glob. Planet.  
863 Change, 148, 181–191, <https://doi.org/10.1016/j.gloplacha.2016.11.014>, 2017.

864 Erion, G., Janizek, J. D., Sturmfels, P., Lundberg, S. M., and Lee, S.-I.: Improving performance  
865 of deep learning models with axiomatic attribution priors and expected gradients, Nat.  
866 Mach. Intell., 3, 620–631, <https://doi.org/10.1038/s42256-021-00343-w>, 2021.

867 Fienen, M. N., Nolan, B. T., and Feinstein, D. T.: Evaluating the sources of water to wells:  
868 Three techniques for metamodeling of a groundwater flow model, Environ. Model. Softw.,  
869 77, 95–107, <https://doi.org/10.1016/j.envsoft.2015.11.023>, 2016.

870 Frame, J. M., Kratzert, F., Klotz, D., Gauch, M., Shelev, G., Gilon, O., Qualls, L. M., Gupta,  
871 H. V., and Nearing, G. S.: Deep learning rainfall–runoff predictions of extreme events,  
872 Hydrol. Earth Syst. Sci., 26, 3377–3392, <https://doi.org/10.5194/hess-26-3377-2022>,  
873 2022.

874 Graves, A., Jaitly, N., and Mohamed, A.R.: Hybrid speech recognition with deep bidirectional  
875 LSTM, in: Proceedings of the 2013 IEEE Workshop on Automatic Speech Recognition  
876 and Understanding (ASRU), IEEE Workshop on Automatic Speech Recognition and  
877 Understanding, Olomouc, Czech Republic, 8–13 December 2013, pp. 273–278, 2013.

878 Gunning, D., Stefik, M., Choi, J., Miller, T., Stumpf, S., and Yang, G.-Z.: XAI—Explainable  
879 artificial intelligence, Sci. Robot., 4, eaay7120,

880 <https://doi.org/10.1126/scirobotics.aay7120>, 2019.

881 Hao, Q., Shao, J., Cui, Y., and Xie, Z.: Applicability of artificial recharge of groundwater in the  
882 Yongding River alluvial fan in Beijing through numerical simulation, *J. Earth Sci.*, 25,  
883 575–586, <https://doi.org/10.1007/s12583-014-0442-6>, 2014.

884 Hersbach, H., Bell, B., Berrisford, P., Biavati, G., Horányi, A., Muñoz Sabater, J., Nicolas, J.,  
885 Peubey, C., Radu, R., Rozum, I., Schepers, D., Simmons, A., Soci, C., Dee, D., Thépaut,  
886 J-N. (2023): ERA5 hourly data on single levels from 1940 to present. Copernicus Climate  
887 Change Service (C3S) Climate Data Store (CDS), DOI: 10.24381/cds.adbb2d47

888 Hochreiter, S., and Schmidhuber, J.: Long short-term memory, *Neural Comput.*, 9, 1735–1780,  
889 <https://doi.org/10.1162/neco.1997.9.8.1735>, 1997.

890 Ireson, A. M., van der Kamp, G., Ferguson, G., Nachshon, U., and Wheater, H. S.:  
891 Hydrogeological processes in seasonally frozen northern latitudes: understanding, gaps  
892 and challenges, *Hydrogeol. J.*, 21, 53–66, <https://doi.org/10.1007/s10040-012-0916-5>,  
893 2013.

894 Jiang, S., Zheng, Y., Wang, C., and Babovic, V.: Uncovering flooding mechanisms across the  
895 contiguous United States through interpretive deep learning on representative catchments,  
896 *Water Resour. Res.*, 58, e2021WR030185, <https://doi.org/10.1029/2021WR030185>, 2022.

897 Jing, H., He, X., Tian, Y., Lancia, M., Cao, G., Crivellari, A., Guo, Z., and Zheng, C.:  
898 Comparison and interpretation of data-driven models for simulating site-specific human-  
899 impacted groundwater dynamics in the North China Plain, *J. Hydrol.*, 616, 128751,  
900 <https://doi.org/10.1016/j.jhydrol.2022.128751>, 2023.

901 Kingma, D. P. and Ba, J.: Adam: A method for stochastic optimization, in: 3rd International  
902 Conference on Learning Representations, 7–9 May 2015, San Diego,  
903 <https://doi.org/10.48550/arXiv.1412.6980>, 2015.

904 Kratzert, F., Klotz, D., Shalev, G., Klambauer, G., Hochreiter, S., and Nearing, G.: Towards

905 learning universal, regional, and local hydrological behaviors via machine learning  
906 applied to large-sample datasets, *Hydrol. Earth Syst. Sci.*, 23, 5089–5110,  
907 <https://doi.org/10.5194/hess-23-5089-2019>, 2019.

908 Li, L., Li, X., Zheng, X., Li, X., Jiang, T., Ju, H., and Wan, X.: The effects of declining soil  
909 moisture levels on suitable maize cultivation areas in Northeast China, *J. Hydrol.*, 608,  
910 127636, <https://doi.org/10.1016/j.jhydrol.2022.127636>, 2022.

911 Liu, Q., Gui, D., Zhang, L., Niu, J., Dai, H., Wei, G., and Hu, B. X.: Simulation of regional  
912 groundwater levels in arid regions using interpretable machine learning models, *Sci. Total  
913 Environ.*, 831, 154902, <https://doi.org/10.1016/j.scitotenv.2022.154902>, 2022.

914 Lundberg, S.M., and Lee, S.-I.: A unified approach to interpreting model predictions, in:  
915 *Advances in Neural Information Processing Systems*, Vol. 30, 31st Annual Conference on  
916 Neural Information Processing Systems (NIPS), Long Beach, CA, 4–9 December 2017,  
917 2017.

918 Lyu, H., Li, H., Zhang, P., Cheng, C., Zhang, H., Wu, S., Ma, Q., and Su, X.: Response  
919 mechanism of groundwater dynamics to freeze–thaw process in seasonally frozen soil  
920 areas: A comprehensive analysis from site to regional scale, *J. Hydrol.*, 625, 129861,  
921 <https://doi.org/10.1016/j.jhydrol.2023.129861>, 2023.

922 Lyu, H., Wu, T., Su, X., Wang, Y., Wang, C., and Yuan, Z.: Factors controlling the rise and fall  
923 of groundwater level during the freezing-thawing period in seasonal frozen regions, *J.  
924 Hydrol.*, 606, 127442, <https://doi.org/10.1016/j.jhydrol.2022.127442>, 2022.

925 Miao, C., Chen, J., Zheng, X., Zhang, Y., Xu, Y., and Du, Q.: Soil water and phreatic  
926 evaporation in shallow groundwater during a freeze–thaw period, *Water*, 9, 396,  
927 <https://doi.org/10.3390/w9060396>, 2017.

928 Nearing, G. S., Kratzert, F., Sampson, A. K., Pelissier, C. S., Klotz, D., Frame, J. M., Prieto,  
929 C., and Gupta, H. V.: What role does hydrological science play in the age of machine

930 learning?, Water Resour. Res., 57, e2020WR028091,  
931 <https://doi.org/10.1029/2020WR028091>, 2021.

932 Niu, X., Lu, C., Zhang, Y., Zhang, Y., Wu, C., Saidy, E., Liu, B., and Shu, L.: Hysteresis  
933 response of groundwater depth on the influencing factors using an explainable learning  
934 model framework with Shapley values, Sci. Total Environ., 904, 166662,  
935 <https://doi.org/10.1016/j.scitotenv.2023.166662>, 2023.

936 Petio, P., Liso, I. S., Pastore, N., Pagliarulo, P., Refice, A., Parise, M., Mastronuzzi, G., Caldara,  
937 M. A., and Capolongo, D.: Application of hydrological and hydrogeological models for  
938 evaluating groundwater budget in a shallow aquifer in a semi-arid region under three  
939 pumping rate scenarios (Tavoliere di Puglia, Italy), Water, 16, 3253,  
940 <https://doi.org/10.3390/w16223253>, 2024.

941 Raghavendra, S. N. and Deka, P. C.: Support vector machine applications in the field of  
942 hydrology: A review, Appl. Soft Comput., 19, 372–386,  
943 <https://doi.org/10.1016/j.asoc.2014.02.002>, 2014.

944 Rahman, A. T. M. S., Hosono, T., Quilty, J. M., Das, J., and Basak, A.: Multiscale groundwater  
945 level forecasting: Coupling new machine learning approaches with wavelet transforms,  
946 Adv. Water Resour., 141, 103595, <https://doi.org/10.1016/j.advwatres.2020.103595>, 2020.

947 Rajaee, T., Ebrahimi, H., and Nourani, V.: A review of the artificial intelligence methods in  
948 groundwater level modeling, Journal of Hydrology, 572, 336–351,  
949 <https://doi.org/10.1016/j.jhydrol.2018.12.037>, 2019.

950 Rui, X.F.: Hydrologic principle, China Water & Power Press, Beijing, China, 386 pp., ISBN:  
951 7-5084-2164-7, 2004.

952 Sarkhel, H. M., Flores, Y. G., Mohammed Al-Manmi, D. A., Mikita, V., and Szűcs, P.:  
953 Assessment of groundwater level fluctuation using integrated trend analysis approaches  
954 in the Kapran sub-basin, North East of Iraq, Groundw. Sustain. Dev., 26, 101292,

955 <https://doi.org/10.1016/j.gsd.2024.101292>, 2024.

956 Singh, A., Nath Panda, S., Flugel, W.-A., and Krause, P.: Waterlogging and farmland  
957 salinisation: causes and remedial measures in an irrigated semi-arid region of India, *Irrig.*  
958 *Drain.*, 61, 357–365, <https://doi.org/10.1002/ird.651>, 2012.

959 Sturmfels, P., Lundberg, S., and Lee, S.-I.: Visualizing the impact of feature attribution  
960 baselines, *Distill.*, 5, e22, <https://doi.org/10.23915/distill.00022>, 2020.

961 Sundararajan, M., Taly, A., and Yan, Q.Q.: Axiomatic Attribution for Deep Networks, in:  
962 *Proceedings of Machine Learning Research*, Vol. 70, 34th International Conference on  
963 Machine Learning, Sydney, Australia, 6–11 August 2017, 2017.

964 Wang, J., Ouyang, W., Liu, X., and Wang, L.: Monitoring hydrological changes with satellite  
965 data: Spring thaw's effect on soil moisture and groundwater in seasonal freezing-thawing  
966 zones, *J. Hydrol.*, 626, Part B, 130365, <https://doi.org/10.1016/j.jhydrol.2023.130365>,  
967 2023.

968 Wang, S., Peng, H., and Liang, S.: Prediction of estuarine water quality using interpretable  
969 machine learning approach, *J. Hydrol.*, 605, 127320,  
970 <https://doi.org/10.1016/j.jhydrol.2021.127320>, 2022.

971 Wang, T., Li, P., Li, Z. B., Hou, J. M., Xiao, L., Ren, Z. P., Xu, G. C., Yu, K. X., and Su, Y. Y.:  
972 The effects of freeze–thaw process on soil water migration in dam and slope farmland on  
973 the Loess Plateau, China, *Sci. Total Environ.*, 666, 721–730,  
974 <https://doi.org/10.1016/j.scitotenv.2019.02.284>, 2019.

975 Wu, C., Zhang, X., Wang, W., Lu, C., Zhang, Y., Qin, W., Tick, G. R., Liu, B., and Shu, L.:  
976 Groundwater level modeling framework by combining the wavelet transform with a long  
977 short-term memory data-driven model, *Sci. Total Environ.*, 783, 146948,  
978 <https://doi.org/10.1016/j.scitotenv.2021.146948>, 2021.

979 Wu, H., Ye, X., Du, X., Wang, W., Li, H., and Dong, W.: Assessing groundwater level

980 variability in response to climate change: A case study of large plain areas, *J. Hydrol. Reg.*  
981 *Stud.*, 57, 102180, <https://doi.org/10.1016/j.ejrh.2025.102180>, 2025.

982 Wu, T., Li, H., and Lyu, H.: Effect of freeze–thaw process on heat transfer and water migration  
983 between soil water and groundwater, *J. Hydrol.*, 617, Part B, 128987,  
984 <https://doi.org/10.1016/j.jhydrol.2022.128987>, 2023.

985 Xie, H.Y., Jiang, X.W., Tan, S.C., Wan, L., Wang, X.S., Liang, S.H., and Zeng, Y.: Interaction  
986 of soil water and groundwater during the freezing–thawing cycle: field observations and  
987 numerical modeling, *Hydrol. Earth Syst. Sci.*, 25, 4243–4257,  
988 <https://doi.org/10.5194/hess-25-4243-2021>, 2021.

989 Xing, Z., Yu, Y., Li, F., Wang, L., Fu, Q., and Wang, H.: Change trend and key influencing  
990 factors identification of main crops water demand in Jiansanjiang, *Trans. Chin. Soc. Agric.*  
991 *Mach.*, 53, 308–315, <https://doi.org/10.6041/j.issn.1000-1298.2022.07.033>, 2022.

992 Xu, L., Cui, X., Bian, J., Wang, Y., and Wu, J.: Dynamic change and driving response of shallow  
993 groundwater level based on random forest in southwest Songnen Plain, *J. Hydrol. Reg.*  
994 *Stud.*, 53, 101800, <https://doi.org/10.1016/j.ejrh.2024.101800>, 2024.

995 Yang, X.: Application of the conceptualization groundwater data model to study the Upper  
996 Arkansas River corridor, Western Kansas, *J. Earth Sci.*, 23, 77–87,  
997 <https://doi.org/10.1007/s12583-012-0234-9>, 2012.

998 Yi, C., Huang, R., Xu, J., Xing, J., and Yi, D.: Dynamic response characteristics of shallow  
999 groundwater level to hydro-meteorological factors and well irrigation water withdrawals  
1000 under different conditions of groundwater buried depth, *Water*, 14, 3937,  
1001 <https://doi.org/10.3390/w14233937>, 2022.

1002 You, N., Dong, J., Huang, J., Du, G., Zhang, G., He, Y., Yang, T., Di, Y., and Xiao, X.: The 10-  
1003 m crop type maps in Northeast China during 2017–2019, *Sci. Data*, 8, 41,  
1004 <https://doi.org/10.1038/s41597-021-00827-9>, 2021.

1005 Zhang, J., Zhu, Y., Zhang, X., Ye, M., and Yang, J.: Developing a Long Short-Term Memory  
1006 (LSTM) based model for predicting water table depth in agricultural areas, *J. Hydrol.*, 561,  
1007 918–929, <https://doi.org/10.1016/j.jhydrol.2018.04.065>, 2018.

1008 Zhao, H.Q. et al.: Investigation and evaluation of groundwater resources and their  
1009 environmental problems in the Songnen Plain, Geological Publishing House, Beijing,  
1010 China, 270 pp., ISBN: 978-7-116-06095-1, 2009.

1011 Zhou, R. and Zhang, Y.: Predicting and explaining karst spring dissolved oxygen using  
1012 interpretable deep learning approach, *Hydrol. Process.*, 37, e14948,  
1013 <https://doi.org/10.1002/hyp.14948>, 2023.